SECURITY CLASSIFICATION OF THIS PAGE

REPORT DOCUMENTATION PAGE

1a. REPORT SECURITY CLASSIFICATION Unclassified	1b. RESTRICTIVE MARKINGS
2a. SECURITY CLASSIFICATION AUTHORITY	3. DISTRIBUTION/AVAILABILITY OF REPORT Approved for public release; distribution is unlimited.
2b. DECLASSIFICATION/DOWNGRADING SCHEDULE	
4. PERFORMING ORGANIZATION REPORT NUMBER(S)	5. MONITORING ORGANIZATION REPORT NUMBER(S)
6a. NAME OF PERFORMING ORGANIZATION Naval Postgraduate School 6b. OFFICE SYMBOL (*If applicable*) 35	7a. NAME OF MONITORING ORGANIZATION Naval Postgraduate School
6c. ADDRESS (*City, State, and ZIP Code*) Monterey, CA 93943-5000	7b. ADDRESS (*City, State, and ZIP Code*) Monterey, CA 93943-5000
8a. NAME OF FUNDING/SPONSORING ORGANIZATION Naval Research Lab 8b. OFFICE SYMBOL (*If applicable*) Code 4110	9. PROCUREMENT INSTRUMENT IDENTIFICATION NUMBER
8c. ADDRESS (*City, State, and ZIP Code*) Washington, D.C. 20375	10. SOURCE OF FUNDING NUMBERS Program Element No: 63207N; Project No: X0513; Task No.; Work Unit Accession Number

11. TITLE (*Include Security Classification*)
Wind Speed and Moisture Sensitivity Tests of the NRL Limited Area Dynamical Weather Prediction Model: An OSSE Study of ERICA IOP-4

12. PERSONAL AUTHOR(S) William J. Schulz, Jr.

13a. TYPE OF REPORT	13b. TIME COVERED	14. DATE OF REPORT (*year, month, day*)	15. PAGE COUNT
Master's Thesis	From To	March, 1992	106

16. SUPPLEMENTARY NOTATION
The views expressed in this thesis are those of the author and do not reflect the official policy or position of the Department of Defense or the U.S. Government.

17. COSATI CODES			18. SUBJECT TERMS (*continue on reverse if necessary and identify by block number*)
FIELD	GROUP	SUBGROUP	Sensitivity tests, prediction model, OSSE

19. ABSTRACT (*continue on reverse if necessary and identify by block number*)

An Observing System Simulation Experiment (OSSE) is conducted to investigate the sensitivity of the Naval Research Laboratory (NRL) mesoscale model to atmospheric water and surface wind speed input. The explosively deepening ERICA IOP-4 storm which occurred off the North Carolina coast on 4 January 1989 is used as a case study. Wind speed and water vapor output from the full physics version of the model is shown to reasonably simulate data available from the Special Sensor Microwave/Imager. Assimilating this modeled satellite information into the degraded version of the model shows ERICA IOP-4 to be a dynamically driven storm.

Assimilation of simulated wind speed observations yields the best performance for the degraded model in terms of surface pressure deepening. The model exhibits sensitivities to the coverage area of updated information. Two treatments for atmospheric water are tested, showing the sensitivity of the model to these inputs despite their secondary importance in forecasts of storm deepening.

20. DISTRIBUTION/AVAILABILITY OF ABSTRACT	21. ABSTRACT SECURITY CLASSIFICATION	
☒ UNCLASSIFIED/UNLIMITED ☐ SAME AS REPORT ☐ DTIC USERS	Unclassified	
22a. NAME OF RESPONSIBLE INDIVIDUAL Teddy R. Holt	22b. TELEPHONE (*Include Area code*) 408-646-2861	22c. OFFICE SYMBOL MR/Ht

DD FORM 1473, 84 MAR 83 APR edition may be used until exhausted
All other editions are obsolete

SECURITY CLASSIFICATION OF THIS PAGE

T258652

Approved for public release; distribution is unlimited.

Wind Speed and Moisture Sensitivity Tests of the NRL Limited Area Dynamical Weather Prediction Model: An OSSE Study of ERICA IOP-4

by

William J. Schulz, Jr.
Lieutenant, United States Navy
B.S., U. S. Naval Academy, 1985

Submitted in partial fulfillment
of the requirements for the degree of

MASTER OF SCIENCE IN METEOROLOGY AND PHYSICAL OCEANOGRAPHY

from the

ABSTRACT

An Observing System Simulation Experiment (OSSE) is conducted to investigate the sensitivity of the Naval Research Laboratory (NRL) mesoscale model to atmospheric water and surface wind speed input. The explosively deepening ERICA IOP-4 storm which occurred off the North Carolina coast on 4 January 1989 is used as a case study. Wind speed and water vapor output from the full physics version of the model is shown to reasonably simulate data available from the Special Sensor Microwave/Imager. Assimilating this modeled satellite information into the degraded version of the model shows ERICA IOP-4 to be a dynamically driven storm.

Assimilation of simulated wind speed observations yields the best performance for the degraded model in terms of surface pressure deepening. The model exhibits sensitivities to the coverage area of updated information. Two treatments for atmospheric water are tested, showing the sensitivity of the model to these inputs despite their secondary importance in forecasts of storm deepening.

536366
C.1

TABLE OF CONTENTS

I. INTRODUCTION 1

A. MOTIVATION 1

B. BACKGROUND-EXISTING THEORIES OF EXPLOSIVE CYCLOGENESIS 3

C. SYNOPTIC DISCUSSION OF THE ERICA IOP-4 CASE STUDY 6

II. TREATMENT OF SATELLITE DATA 13

A. SENSOR CONFIGURATION AND ALGORITHMS 13

1. Wind Speed Algorithm 16

2. Water Vapor Algorithm 17

B. ERROR SOURCES IN THE SSM/I DATA 21

III. MODEL DESCRIPTION 24

A. DESCRIPTION OF NRL MODEL 24

B. MODEL STRUCTURE 25

C. TIME INTEGRATION 26

D. CUMULUS PARAMETERIZATION 27

E. MODIFICATIONS TO THE MODEL 28

IV. OBSERVING SYSTEM SIMULATION EXPERIMENT (OSSE) DESIGN 32

A. COMPARISONS OF SSM/I IMAGES AND 16 LAYER MODEL OUTPUT 32
1. Satellite Data 32
2. Wind Speed 33
3. Water Vapor (Total Precipitable Water) . . . 41
B. EXPERIMENT DESIGN 49
1. OSSE 49
2. Analysis plan 51
C. SERIES I: COINCIDENTAL FOUR PERIOD NUDGING . . 53
D. SERIES II: MOISTURE ASSIGNMENT AND DISTRIBUTION 57
E. REMAINING SERIES 58
1. Centered Four-Period Assignments 58
2. "Polar Orbiter" Simulator 59
F. FINAL COMMENTS 59

V. ANALYSIS OF RESULTS 60
A. OVERVIEW 60
B. COMPARISON OF SENSITIVITY TEST RESULTS 60
C. SERIES I: SWATH VS. DOMAIN WIND ASSIMILATION . 61
D. MOISTURE SENSITIVITY 70
1. Domain vs. Swath Comparison 70
2. Surface Only vs. Vertical Moisture Distribution 79
E. TIME SENSITIVITY 83

F. INDIVIDUAL PARAMETER COMPARISONS IN THE POLAR ORBITER SIMULATION 86

VI. CONCLUSIONS AND RECOMMENDATIONS 99

A. CONCLUSIONS 99

B. RECOMMENDATIONS 101

LIST OF REFERENCES 102

INITIAL DISTRIBUTION LIST 105

LIST OF TABLES

TABLE 1. WIND SPEED ACCURACIES BASED ON RAIN FLAGS (Hollinger et al., 1989) 17

TABLE 2. SSM/I PARAMETER ERRORS 23

TABLE 3. SUMMARY OF EXPERIMENTS 51

LIST OF FIGURES

Figure 1. Storm track and central pressure of ERICA IOP-4 storm, 4 January 1989 7

Figure 2. NMC analyzed surface pressure (solid lines, mb) and 1000-500 mb thickness (dashed, dm) at 0000 UTC 4 January 1989. 9

Figure 3. SSM/I 37 GHz and 85 GHz channels beam footprints within a swath for various angles from the nadir (Hollinger et al., 1987). 15

Figure 4. Wind speed accuracies based on SSM/I rain flags for the 0000 UTC swath. 18

Figure 5. Wind speed accuracies as in Figure 4, but for the 0930 UTC swath. 19

Figure 6. Wind speed accuracies as in Figure 4, but for the 2200 UTC swath. 20

Figure 7. NRL Mesoscale Model domain. 30

Figure 8. SSM/I wind speed (m/s) at 0000 UTC. 34

Figure 9. SSM/I wind speed (m/s) at 0930 UTC. 35

Figure 10. SSM/I wind speed (m/s) at 2200 UTC. 36

Figure 11. EE16 generated surface wind field (m/s) at 0600 UTC. 37

Figure 12. EE16 generated surface wind field (m/s) at 1200 UTC. 38

Figure 13. EE16 generated surface wind field (m/s) at 1800 UTC. 39
Figure 14. EE16 generated surface wind field (m/s) at 2400 UTC. 40
Figure 15. SSM/I water vapor image at 0000 UTC. Contours depict precipitable water amounts in kg/m^2. 42
Figure 16. As in Figure 15, but at 0930 UTC. 43
Figure 17. As in Figure 15, but at 2200 UTC. 44
Figure 18. EE16-generated precipitable water (x 10 kg/m^2) at 0600 UTC. 45
Figure 19. As in Figure 18, but for 1200 UTC. 46
Figure 20. As in Figure 18, but at 1800 UTC. 47
Figure 21. As in Figure 18, but at 2400 UTC. 48
Figure 22. Sensitivity test summary. Asterisks indicate update points using EE16 data. Numbers below asterisks indicate generation time of update information by EE16. 54
Figure 23. Vertical weighting function for conversion of 16 Layer data to 10 Layers. 56
Figure 24. Series I storm development. 62
Figure 25. TW1/SW1 isotachs, in m/s, at 1200 UTC. . . 64
Figure 26. TW1/SW1 surface pressure (solid lines, mb) and temperature (dashed, ^0C) at 2400 UTC. 65
Figure 27. TW1/SW1 isotachs (m/s) at 2400 UTC. 66

Figure 28. Warm front cross section of omega (microbars/sec) for TW1 at 2400. "A" and "B" correspond to points on Figure 26. 68
Figure 29. As in Figure 28, but for SW1. 69
Figure 30. Series I surface wind RMS errors. 71
Figure 31. SW1 vs. TW1 storm tracks. 72
Figure 32. Precipitable water content (x10 kg/m^2) for TM2 and SM2 at 2400 UTC. 74
Figure 33. Series II storm development. 75
Figure 34. SM2/TM2 surface pressure (solid, mb) and temperature (dashed, ^0C) at 2400 UTC. 76
Figure 35. 24 hour accumulation of precipitation (cm) for TM2. Contour interval is 10 cm. 77
Figure 36. Series II 500 mb wind speed error. 78
Figure 37. Series II 500 mb moisture RMS error. . . . 80
Figure 38. TV2/TM2 900 mb winds (m/s) at 1800 UTC. . . 82
Figure 39. TV3 700 mb vorticity (x$10^{-5}s^{-1}$) at 1800 and 2400 UTC. 84
Figure 40. As Figure 39, but for TV2. 85
Figure 41. Series IV storm development. 87
Figure 42. TW4 surface pressure (solid, mb) and temperature (dashed, ^0C) at 0600 UTC. 88
Figure 43. Surface pressure (solid, mb) and temperature (dashed, ^0C), TW4 at 2400 UTC. 91
Figure 44. TM4 surface pressure (solid) and temperature (dashed), 2400 UTC. 92

Figure 45. TV4 surface pressure (solid) and temperature (dashed), 2400 UTC. 93
Figure 46. Series IV 850 mb temperature RMS errors. . 94
Figure 47. Series IV 500 mb moisture RMS errors. . . . 95
Figure 48. Series IV 850 mb moisture RMS errors. . . . 97
Figure 49. Series IV 500 mb wind RMS errors. 98

ACKNOWLEDGMENTS

Grateful appreciation goes out to Assistant Professor Teddy Holt for his patience and enthusiasm. Special thanks are also due Professor Carlyle Wash for his most helpful direction in interpreting satellite information. On the hardware side, Craig Motell and Jim Cowie provided essential guidance as to the inner workings of the NPS IDEA Lab.

Valuable guidance on SSM/I data and algorithm usage was provided by J. Hollinger and G. Sandlin of the Naval Research Laboratory. This research was partially funded by the Naval Research Laboratory, Washington, D.C., under project number X0513.

Finally, thanks to Jennifer and Amanda for providing needed moral support and enduring the long hours with me.

I. INTRODUCTION

A. MOTIVATION

To improve numerical weather prediction, satellite data needs to be assimilated with other model inputs. Efficiently incorporating these remote observations into numerical weather prediction models improves forecasts by bridging the gap between simulation and the real world. Problems arise in marrying a sensor of fixed temporal and spatial resolution to a model whose stability requirements dictate a specific finite resolution scheme. The objective of this study is to examine the potential for incorporation of DMSP Special Sensor Microwave/Imager (SSM/I) data into the Naval Research Laboratory's Limited Area Dynamical Weather Prediction Model. Products to be tested include SSM/I derived wind speed and atmospheric water content. The case study to be examined is an explosive storm occurring on 4 January 1989, part of the Experiment on Rapidly Intensifying Cyclones over the Atlantic, Intensive Observation Period Four (ERICA IOP-4). Operational models failed to predict this storm's extreme deepening rate of 60 mb in 24 hours. By nudging the modeled development of this storm with information derived from the simulation of three SSM/I passes, a prediction closer to the final intensity of the storm,valid at 0000 UTC 5 January 1989, may be obtained.

Post-storm analysis (Sanders, 1990) places the 0000 UTC 5 January pressure of the storm at 936 mb, while the National Meteorological Center (NMC) analysis gives a value of 956 mb. A disparity evolves between the predictions and the actual storm as development progresses. The widening gap motivates inquiry into the most important factors in the storm's rapid development, and the possibility of effectively simulating satellite observations.

The SSM/I is an excellent candidate for providing observed values for validation and improvement of model predictions. Fully operational, the SSM/I provides reliable atmospheric water parameters suitable for operational forecasting (Alishouse et al., 1990a). The improved non-linear algorithm has been validated by radiosonde observations, and shows marked sensitivity to cloud liquid water content, rain and sea ice. Cloud liquid water has been validated by the NOAA-WPL profiler network (Alishouse et al., 1990b). While not reliable over land, the derived algorithm is highly effective at determining marine cloud liquid water. For the North Atlantic Ocean domain used in this study, the data provided is suitable. The SSM/I also provides surface wind speed over the ocean based on wave structure and foam coverage. The information is usable in the modeling case, but wind speed data is not as accurate as other parameters (Hollinger, 1991). Sources of SSM/I error will be discussed in Chapter II.

The SSM/I's ability to provide global, day and night observations make it a potentially important model input. Use of microwave imagery is advantageous since microwaves penetrate cloud coverage. Microwaves are independent of solar illumination, and are readily comparable with visible and infrared images (Hollinger and Sandlin, 1990). Microwave transmission is sensitive to the physical state of water in the atmosphere, dependent upon humidity, clouds and rain. Proven operational use of SSM/I data includes the marine weather updates covering the approach of Hurricane Hugo, which incorporated 3-hour old SSM/I wind speeds. Fleet Numerical Oceanography Center (FNOC) also produces SSM/I derived wind speed fields. The Naval Research Laboratory-West (NRL-West, formerly the Naval Environmental Prediction and Research Facility, NEPRF) has concluded that SSM/I wind speeds are equivalent in quality to ship reported winds, and is now attempting to successfully assimilate these winds into NOGAPS (Goerss, 1988). Data collection has begun with the SSM/I follow on platform, the SSM/T2 atmospheric sounder.

B. BACKGROUND-EXISTING THEORIES OF EXPLOSIVE CYCLOGENESIS

While not a comprehensive review of the subject, several theories on aspects of cyclogenesis that can provide the impetus for an explosive event are mentioned here to provide direction in the post experiment analysis. Fosdick and Smith (1991) have listed processes previously identified as

important to explosive cyclones, or "bombs." These include upper level cyclonic vorticity advection, upper level divergence associated with a well defined jet streak, boundary layer fluxes of heat and moisture, latent heat release and low static stability as a precursor to development. Their synoptic discussion of an explosive storm developing in roughly the same area is considered here. The initial setting consisted of a surface low in a strong baroclinic zone downstream of a large amplitude upper level trough, near the entrance region of a jet maximum. Midway through the explosive phase, strong low-level thermal advection was occurring within the cyclonic circulation. By the end of the explosive phase, this thermal advection had extended southwest and northeast of the center.

The precipitation pattern of the Fosdick and Smith storm changed according to the phase of the storm. At the beginning of the explosive phase, precipitation was predominantly convective and located in the warm sector. At the midpoint of the explosive phase, amount and areal coverage of precipitation had increased. Precipitation was now a maximum over the low and still mostly convective. Relating the amount of rainfall to latent heat release, Fosdick and Smith were able to draw conclusions about the importance of latent heat release on explosive cyclogenesis. Latent heat release contributed to height falls below the level of maximum heating. Latent heat release accounted for 33% of total

development at 700 mb. Lowering the level of maximum heating increases cyclone development.

Studies of interaction between baroclinic and diabatic processes suggest that a nonlinear relationship exists between latent heat release and rapid development (Kuo et. al, 1991). Kuo et al.'s study of the QEII storm showed the surface cyclone related to quasi-geostrophic forcing of a mid-tropospheric short wave trough for periods of greater than 12 hours. Development was also associated with intense mid-level and upper-level vorticity maxima. Moist frontogenesis contributed to rapid marine cyclogenesis. The conclusion of Kuo et al.'s study was that rapid cyclogenesis must be viewed in the context of moist baroclinic instability with strong nonlinear interaction between dynamic and diabatic processes.

Varying the treatment of atmospheric moisture can have a distinct impact on model predictions. In a study of nine Western Atlantic cyclones, the Arakawa-Schubert scheme gave deeper, more realistic deepening rates than the Kuo convective parameterization scheme (Kuo and Low-Nam, 1990). Precipitation is driven by mesoscale slantwise ascent in the vicinity of the warm front in a rapidly deepening cyclone. In concurrence with the previously discussed studies, latent heat release (LHR, here associated with the sloping frontal cloud band) promotes frontogenesis and increased low-level vorticity when LHR interacts with adiabatic frontal circulation. Models which can determine LHR from internal dynamics should give

better results than models using arbitrarily prescribed parameterization schemes (Kuo and Low-Nam, 1990). Thus, using simulated observations of precipitation to drive latent heating release rates should improve model simulations. A further result of the Kuo study was that significant amounts of water vapor were needed in the initial stages to support rapid deepening.

Kuo and Low-Nam's conclusion that dynamically formed cyclones are more easily predicted than diabatically formed storms is supported by studies based on NMC's Nested Grid Model. Sensitivity tests using the NGM Model examining the role of latent heat release in IOP-4 attributed 27% of its deepening to latent heat release, suggesting that the storm was primarily driven by dynamics probably associated with the strong short wave aloft (Pauley et. al, 1991).

C. SYNOPTIC DISCUSSION OF THE ERICA IOP-4 CASE STUDY

The ERICA IOP-4 storm of 4-5 January 1989 was the deepest cyclone occurring during the ERICA project (Hartnett et. al, 1989). Between 0900 and 1500 UTC (all times given are 4 January 1989 unless specified) the storm deepened at the explosive rate of 24 mb in 6 hours, enroute to a final estimated pressure of 936 mb. Figure 1 presents the storm's deepening rate and low pressure center track. The IOP-4 storm was the trailer of a pair of storms depicted in Figure 2. Rapid

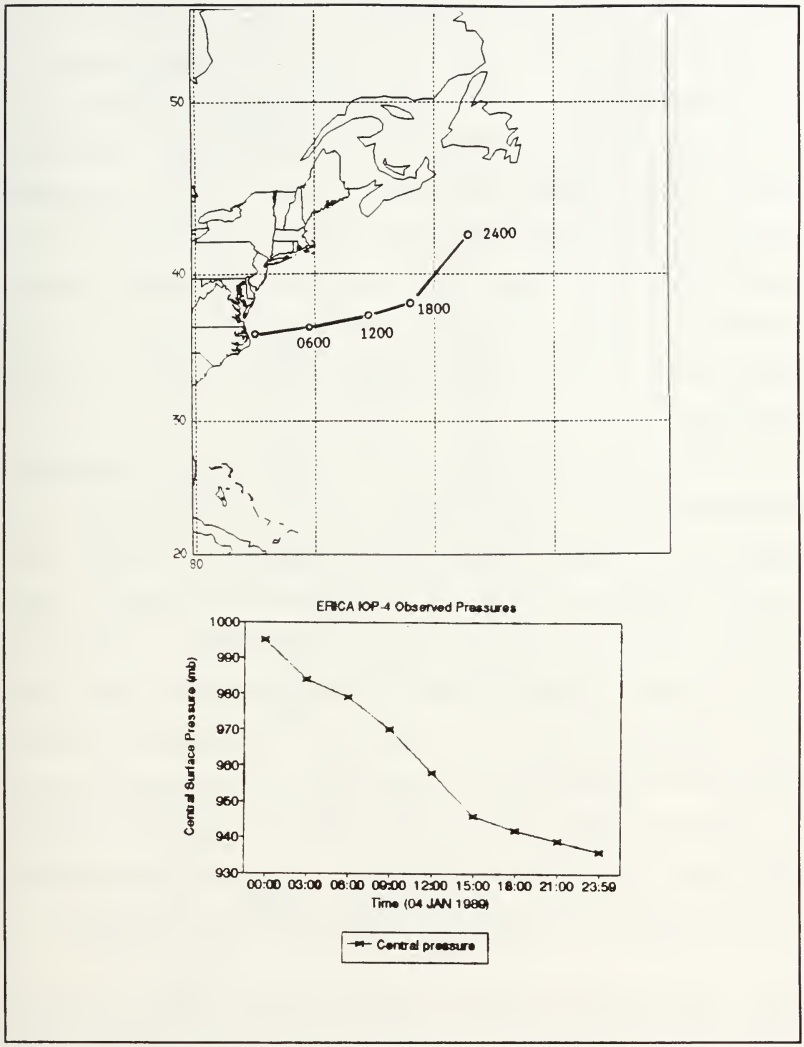

Figure 1. Storm track and central pressure of ERICA IOP-4 storm, 4 January 1989

deepening occurred immediately upon upper air forcing reaching the coastline at 0000 UTC. Strong mesoscale development in the cyclone interior during the explosive phase resulted in a tight cloud band surrounding the clear center. Satellite imagery implied that development began in the northwest quadrant of the cyclone around several equally strong low pressure centers at 1200 UTC. These centers made a partial revolution around the previous cyclone center. The intensification of this low coincided with the period of most rapid deepening.

A detailed discussion of synoptic and mesoscale characteristics of the storm lays the groundwork for comparison of model experiments. Evolution of sea level pressure deepening began with a 996 mb low east of Cape Hatteras, North Carolina (Nieman et al., 1991). Warm and moist air over the Gulf Stream was separated from cooler and drier continental air over the coastal plain by a coastal trough extending southwestward from the cyclone center (Figure 2). Intensification began as a surface cold front, coupled with an upper level jet-front system, advanced from the west. Strong southwesterly winds developed east of the coastal

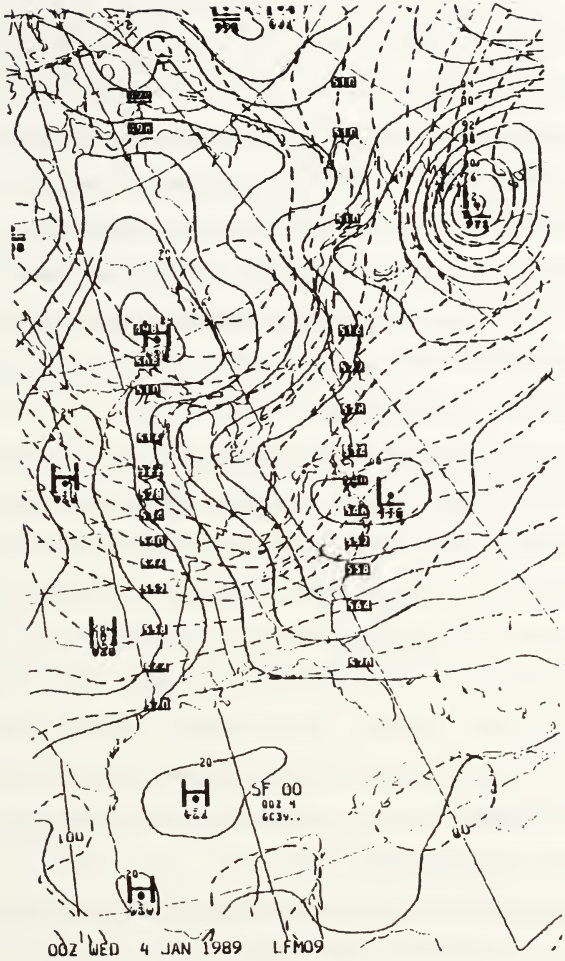

Figure 2. NMC analyzed surface pressure (solid lines, mb) and 1000-500 mb thickness (dashed, dm) at 0000 UTC 4 January 1989.

trough in the Gulf Stream boundary layer due to mixing of higher momentum aloft downward. These strong southwesterly winds combined with negative air-sea temperature differences contributed to combined sensible and latent heat fluxes of 1500 W/m^2 upwards from the ocean surface. Ahead of the cold front, a deep convective cloud line developed over the upward heat fluxes. The resulting flow transported warm moist air northward toward the warm frontogenesis region. Cyclogenesis commenced beneath the 500 mb flow and strong 700 mb ascent (Nieman et. al, 1991).

Due to the linear pressure drop shown in Figure 1, Niemann et. al could not identify a prominent deepening phase. In the first 6 hours of the case study, the intensifying cyclone was centered near the triple point, while an incipient bent-back frontal feature was developing to the west. The mesoscale cyclone continued to trail farther and farther behind the triple point and deeper into the polar air stream. The cyclone exhibited a scale and structure similar to polar low type cyclogenesis as it propagated from the southwest in a reverse shear environment.

Following temperature evolution at 850 mb, Neiman et. al. were able to identify four phases of frontal evolution developed by Shapiro and Keyser (1990). Specifically;

1. Broad Baroclinic phase
2. Frontal Fracture phase

3. T-bone phase, and

4. Warm Seclusion phase

The broad east-west baroclinic zone present at 0000 UTC supported incipient cyclogenesis. By 0600 UTC progress of the second phase was evident as the warm and cold fronts were distinctly fractured at the triple point. At 1200 UTC, a T-bone frontal configuration developed consisting of the north-south oriented cold front intersecting the east-west warm front. Finally, between 1800 UTC and 0000 UTC 5 January, the cyclone attained its lowest pressure and maximum vorticity in the warm core seclusion phase. Cold polar air nearly encircled the cyclone center by 0000 UTC (5 January), secluding a warm pocket near the low center. At the end of the period, the outward sloping bent-back occlusion was distinguishable through 500 mb, although it weakened with height (Niemann et. al, 1991).

Flight level observations documented mesoscale features, producing temperature and streamline data. Based on cross-sectional analysis, the 0600 UTC cold front was nearly vertical below 800 mb. Cold front convective bands contained 20 km scale eddies and periodic gaps in the along-front direction. The warm front consisted of a steep leading edge with a positive isentropic potential vorticity anomaly at the leading edge of the front. Radar cross-sections revealed a shallow slope along the warm front while under stratiform

precipitation, and a nearly vertical slope in the vicinity of the mesoscale convective elements. Vertical portions of the front displayed enhanced cross-frontal convergence.

Streamline analysis from the same aircraft data shows strong confluence along the warm convective band, with weaker confluence aligned with the cold frontal band. The primary cyclone center at 0600 UTC was located in the closed circulation approximately 40 km west of the triple point. A secondary circulation center existed 125 km west of the triple point along the bent-back front. The analysis clearly displays multiple vortices during the early stage of cyclogenesis. One of the objectives of this study is the investigation of how assimilation of satellite data can improve the model's description of these features.

II. TREATMENT OF SATELLITE DATA

A. SENSOR CONFIGURATION AND ALGORITHMS

The Special Sensor Microwave/Imager flies on board the Defense Meteorological Satellite Program (DMSP) block 5D-2 spacecraft F8, operational since 1987. The spacecraft orbits at 833 km in a sun-synchronous, near polar orbit resulting in a 1400 km swath width. The sensor consists of a seven channel, four frequency (19.35, 22.235, 37.0 and 85.5 GHz), linearly polarized passive microwave radiometric system. Continuous rotation at 31.6 RPM about a vertical axis allows the sensor to measure brightness temperatures over a 102.4° angular sector. The imaging scanner operates left to right. During each scan, 128 radiometric samples are taken at the two 85.5 GHz channels, with 64 samples taken on alternating scans at the remaining five lower frequency channels (Hollinger et al., 1987).

Scan geometry will influence the nature of geolocation error in an SSM/I image. The satellite track moves along the Y-direction at 6.58 km/sec, rotating about the vertical as described. This results in a separation distance between successive scans of 12.5 km along the track, which is nearly the resolution of the 85.5 GHz channels. Using a sampling interval of 4.22 msec (the time for the beam to travel 12.5 km

across the track) increases the along-scan beam diameter. As a result, the 85.5 GHz beam is nearly circular. The lower frequency channels sample at a 8.44 msec interval on alternating scans. Figure 3 depicts the footprint of beams in a swath, indicating that beam overlap occurs predominantly at the edge of the swath (Hollinger et al., 1987).

Beam inefficiency coupled with scan geometry contributes to SSM/I error. The most efficient beams (beams having the highest concentration of energy in a 3 dB bandwidth) are the 19.35 GHz channels. The vertical beam is 96.1% efficient, and the horizontal is 96.5% efficient. Least efficient is the 85.5 GHz horizontal, calculated at 91.1% based on the deployment of antenna components, alignment of the sensor with the spacecraft, and feedhorn design. NRL computations have determined an along beam pointing accuracy of 5.3 km, and a cross track accuracy of 3.2 km, both less than the 85.5 GHz beam half width (Hollinger et al., 1987).

Noise Equivalent Temperature Differential (NE▲T) represents the radiometer sensitivity. To reduce radiometer gain fluctuation and, subsequently, NE▲T, the instrument undergoes a radiometric calibration every 1.19 seconds. Calibration is done by passing the feedhorn beneath two fixed calibration reference targets, a 300K hot receiver and a 3K cold cosmic background view. Scene incident temperature is a linear function of these calibration readings and received brightness temperatures. Five samples from each scan are

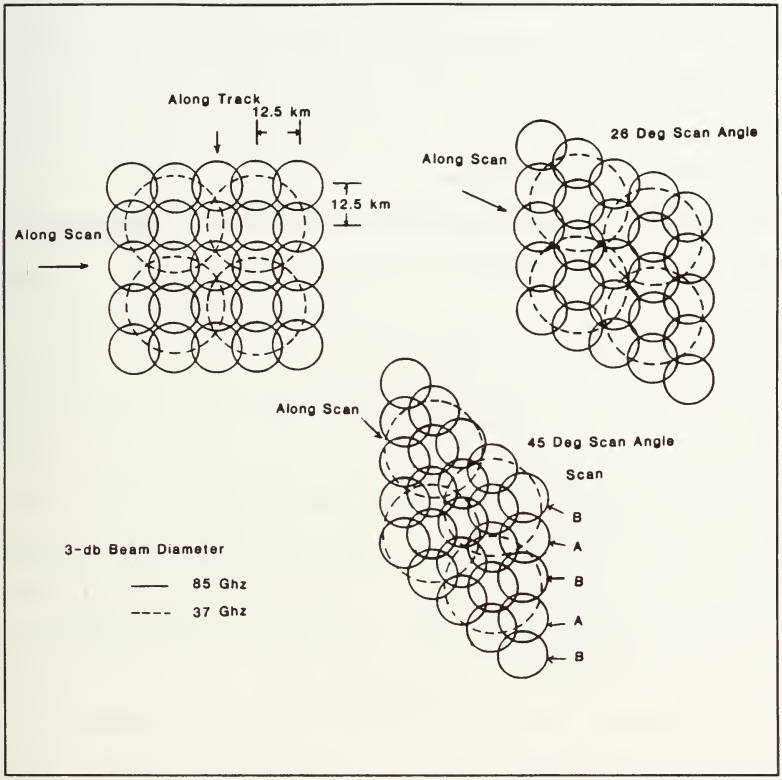

Figure 3. SSM/I 37 Ghz and 85 Ghz channels beam footprints within a swath for various angles from the nadir (Hollinger et al., 1987).

averaged to reduce noise estimates in hot and cold load readings. Calibration parameters are updated on each scan to compute scene brightness temperatures. The accuracy of scene brightness temperatures incident on the reflector can improve with several corrections applied. These corrections account for feedhorn spillover, cross polarization coupling and sidelobe contribution.

1. Wind Speed Algorithm

The recommended surface wind speed algorithm is linear, with varying degrees of accuracy (Hollinger, 1991):

$$SW = 147.90 + 1.0969 * T_{B19V} - 0.455 * T_{B22V} - 1.76 * T_{B37V} + .7860 * T_{B37H}$$

where SW is wind speed in meters per second. Typical wind speed errors are near 2 m/s. T_{B19V}, T_{B22V}, and T_{B37V} are the brightness temperatures in the 19 GHz, 22 GHz and 37 GHz vertically polarized beams. T_{37H} is the brightness temperature in the 37 GHz horizontally polarized beam.

Microwave radiation, particularly at the lowest three frequencies of the SSM/I, is heavily attenuated by rain, which in turn dampens the wave-generated wind speed signature. Table 1 lists rain rate dependent wind speed accuracies. Accuracy of the wind speed retrieval drops off severely with rain due to sensor frequency limitations, not algorithm

TABLE 1. WIND SPEED ACCURACIES BASED ON RAIN FLAGS (Hollinger et al., 1989)

Rain Flag	Criteria	Accuracy
0	$T_{37V}-T_{37H} > 50$ AND $T_{19H} < 165$	< 2 m/s
1	$T_{37V}-T_{37H} < 50$ OR $T_{19H} > 165$	2-5 m/s
2	$T_{37V}-T_{37H} < 37$	5-10 m/s
3	$T_{37V}-T_{37H} < 30$	> 10 m/s

problems. (Hollinger, 1989)

Figures 4, 5, and 6 show the rain flag distribution and geographic position of the three swaths. The most severe wind speed error in this case study is 5 m/s.

2. Water Vapor Algorithm

The recommended water vapor (total precipitable water) retrieval algorithm is non-linear in 22 GHz (Hollinger, 1991):

$$WV=232.89393-.148596*T_{19_v}-1.829125*T_{22_v}+.006193*(T_{22_v})^2$$

$$-3.6954*T_{37_v}$$

where WV is the total precipitable water in kilograms per square meter. This algorithm results from regression of international radiosonde network data. Typical errors in total precipitable water are within 2.4 kg/m^2.

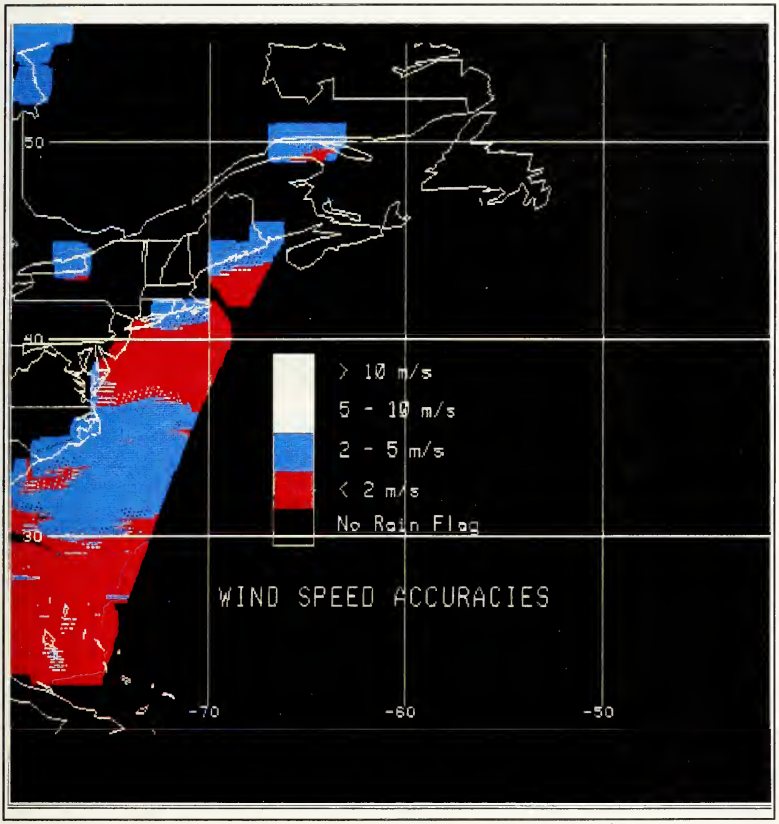

Figure 4. Wind speed accuracies based on SSM/I rain flags for the 0000 UTC swath.

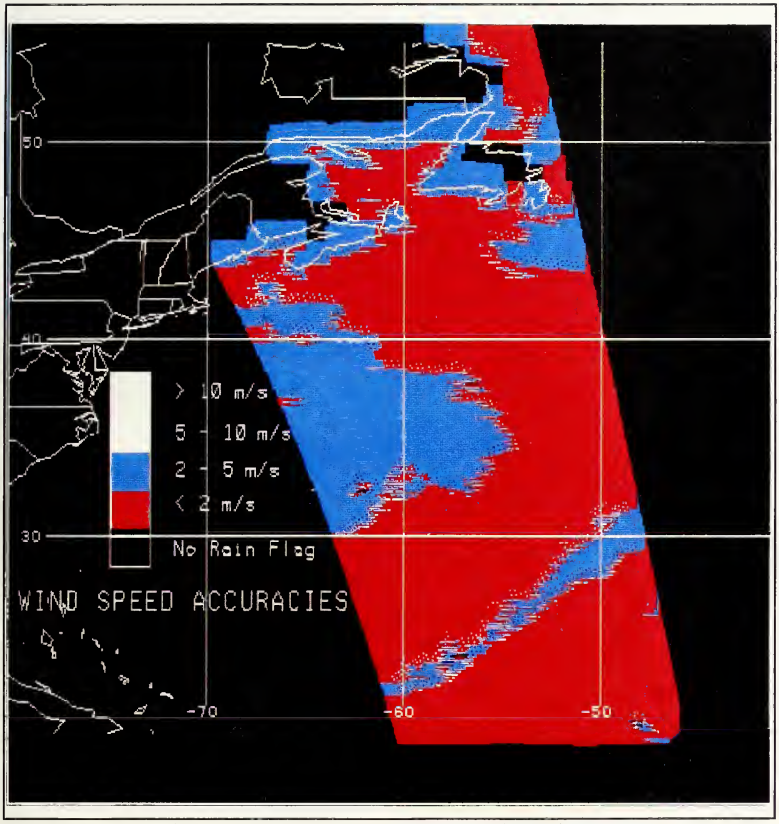

Figure 5. Wind speed accuracies as in Figure 4, but for the 0930 UTC swath.

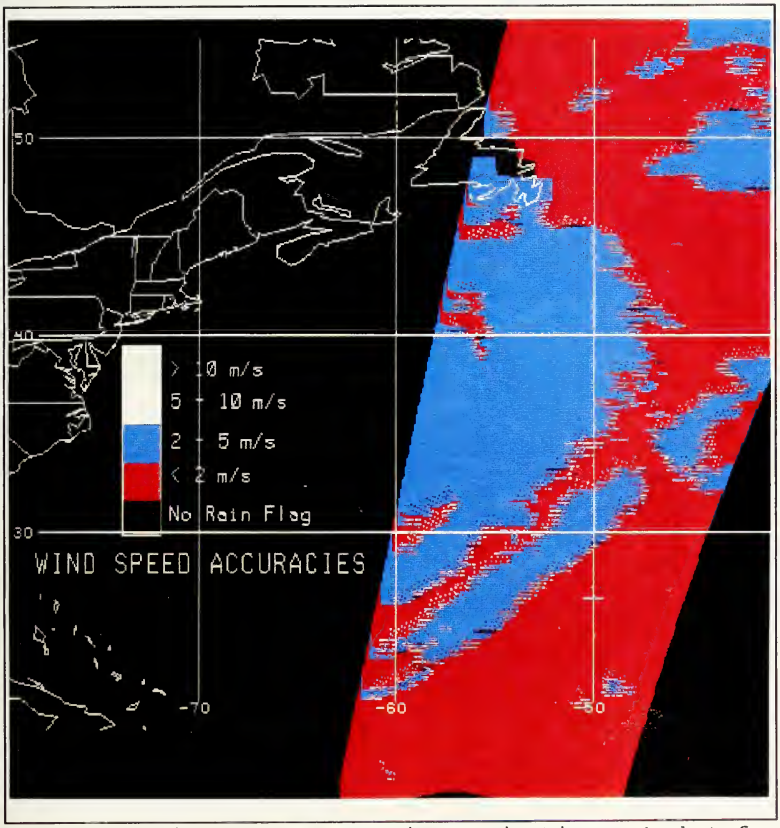

Figure 6. Wind speed accuracies as in Figure 4, but for the 2200 UTC swath.

The validation report (Hollinger, 1991) recommends employment of a precipitation screen prior to computing water vapor over the ocean. Application of this screen obliterates most of the image, while neglecting this screen gives useful structural information. In the unscreened image, however, the magnitudes of precipitable water are much higher than the NRL model predictions, as discussed in Chapter IV.

B. ERROR SOURCES IN THE SSM/I DATA

The SSM/I was designed to meet an operational spatial resolution requirement of 14 km. However, the sensor has not always performed to this standard, displaying errors up to 30 km near coastlines. The sensor's geolocation algorithm assumes that the spacecraft is always perpendicular to the earth-satellite vertical, and that the earth is a perfect oblate spheroid. Errors can be induced by many elements, including:

- Spacecraft orbital elements
- Spacecraft ephemeris data
- Sensor pixel location algorithm
- Sensor deployment/alignment of spin axis
- Sensor alignment to spacecraft
- Spacecraft altitude

Also included are errors in maps to which the satellite data must be compared (Poe and Conway, 1990).

Orbital element errors, errors in the set of parameters defining the size, shape and orientation of the orbit, are small contributors to SSM/I geolocation error. Comparisons of NORAD and NAVSPASUR data indicate the orbital elements contribution to be less than 1.5 km. (Poe and Conway, 1990). Errors in the satellites tabulated position (ephemeris) are less than 3 km as computed by contrasting FNOC and NORAD models. Comparisons of FNOC and NORAD data displayed a 13 km subsatellite position difference coincident with FNOC's dataset update time. This indicates the scale of the error induced by the data collection process. Further comparisons with ephemeris data from the U.S. Air Force 1000th Space Operations Group (1000th SOG) indicate differences between spacecraft and FNOC ephemeris can be as large as 15 km (Hollinger, 1991).

The geolocation algorithm employs many numerical approximations to reduce the computer processing load. This induces a small error in the satellite's tabulated position. Total error from this source does not exceed 4 km.

The final NRL Calibration/Validation study of SSM/I data used the 85 GHz channel to study geolocation error in SSM/I derived images. This channel provides the best spatial resolution, 12 km. The largest geolocation error offsets the data 20 to 30 km in the eastern Mediterranean Sea, with common

smaller errors (15-20 km) existing near coastlines in the Red Sea. Computational methods have been proposed to reduce the errors to 1 to 3 km, but these processes have not been employed pending further testing with more extensive data sets. (Hollinger, 1991). Table 2 summarizes SSM/I error estimates.

TABLE 2. SSM/I PARAMETER ERRORS

SSM/I ERROR		CHANNEL RESOLUTION	
Orbital Elements	1 km	85 GHz	12 km
Ephemeris	15 km	37 GHz	27.7 km
Approximations	4 km	22 GHz	46.5 km
Total Geolocation error	20 km	19 GHz	54 km
SW/TPW algorithm error		20 + 27.7	= 47.7 km

III. MODEL DESCRIPTION

A. DESCRIPTION OF NRL MODEL

The NRL Limited Area Dynamical Weather Prediction Model accurately depicts processes and characteristics of the lower troposphere (Madala et al., 1987). Using quasi-hydrostatic sigma coordinates permits reasonable modeling of baroclinic development. Other physical processes, notably cumulus convective heating, are parameterized. A brief description of the model provides a framework for understanding the structure of the sensitivity tests, which are described in Chapter IV.

The model employs the Arakawa C-grid since that scheme presents several physical advantages (Arakawa and Lamb, 1977). The C-grid best simulates the geostrophic adjustment process, which influences how the primitive equation system responds to ageostrophic initial conditions. When initial conditions specify an imbalanced region, gravity waves propagate out of that anomalous region. Use of the C-grid also conserves the integral properties of the atmosphere. Staggering the grid permits the separation of various waves by phase speed.

At specified mass points on the grid, the quantities temperature, geopotential, specific humidity, and sigma are computed. U-velocity (east-west) is computed midway between latitudinal grid points, while v-velocity (north-south) is

computed midway between longitudinal grid points. The seven governing equations employed in the model are:

- U-momentum
- V-momentum
- Thermodynamic equation
- Moisture continuity equation
- Surface Pressure Tendency
- Hydrostatic equation
- Continuity equation

Integration of these seven equations over time by a split-explicit method generates the state variables. Use of the split-explicit scheme provides for separation of components into Rossby and Gravity wave modes. The primitive equations must be written in matrix form to achieve an eigenvector solution whose elements will satisfy the various propagation speed requirements (Madala et al., 1987).

B. MODEL STRUCTURE

The main program calls several subroutines, each of which computes a state variable, a correction term, or paramaterizes a physical process. The objective of the program is the forecasting of meridional wind, zonal wind, temperature, surface pressure, geopotential height and sigma for the five prognostic and two diagnostic equations. From the initialization state chosen by the user, the model reads

fields of the wind components, air temperature, sea surface temperature, moisture, sea level pressure and boundary layer parameters. The eigenvector solutions that result from solving matrix forms of the primitive equations provide pressure gradient and divergence correction terms. Separate subroutines compute mass divergence, geopotential corrections, diffusion and Monin-Obukov boundary layer parameters.

Of particular interest in this study, the subroutine CUPARA determines cumulus convection based on a modified Kuo scheme. According to this algorithm, convection exists only when the total moisture required for cloud formation is positive (Kuo, 1974). This depends on cloud-environment temperature and moisture differences. New environmental values of temperature and humidity are fed back to the main program. In the absence of convective heating, stable heating is indicated if the relative humidity is greater than 96% (Holt et al, 1990). Section D describes in greater detail the flow of the cumulus parameterization.

C. TIME INTEGRATION

Gradient processes in the atmosphere potentially trigger gravity wave disturbances. These disturbances are low amplitude waves with little energy that require a small time step if they are to be captured by the model. Deviation terms in divergence and pressure tendency contain elements that vary over the time scale of Rossby waves and require a larger time

step for proper modeling. The split-explicit method handles both wave scales by dividing the time step into sub-intervals and carrying out explicit integration within each sub-interval. Employment of this scheme in a three dimensional model in grid point space runs into practical difficulties (Madala et al., 1987).

On the grid, the array of gravity waves modes satisfy an array of CFL criteria. Each physically occurring gravity wave requires a different time step, as do the natural modes generated by the numerical model (one at each level). Fortunately, the natural gravity modes form a complete set of eigensolutions to the boundary conditions. This set of solutions can be accounted for with constants, allowing variation of the dependent variables to be expressed as linear combinations of the structure functions (Madala et al., 1987).

D. CUMULUS PARAMETERIZATION

The cumulus parameterization subroutine defines convection and adjusts the state variables of temperature and moisture where cumulus convection exists. For this subroutine the model is strongly dependent on the initial magnitudes and distributions of the "observed" state values. In CUPARA, weighting functions for vertical heating as well as moisture divergence are computed for each model level. After vertical integration, the derived total moisture convergence (divergence) is added to any supersaturation that may have

occurred in the lowest level of the modeled atmosphere. Saturation vapor pressure, saturation specific humidity and relative humidity are derived for each level, as well as temperature and specific humidity at points of upward vertical velocity. Comparison of all levels yields the vertical gradient of moist stable energy.

If the required amount of moisture to form clouds exists and the atmosphere is unstable, convective heating and clouds are indicated. When relative humidity exceeds 95%, no additional moisture is placed into the surrounding environment. Finally, the subroutine computes the change in temperature and humidity due to the mixing of clouds in the environment (Madala et al., 1987).

E. MODIFICATIONS TO THE MODEL

For this study the model domain focuses on the western Atlantic Ocean, bounded by 20°-55° N and 40°-80° W as shown in Figure 7. The numerical grid consists of a 136 by 141 point horizontal plane (1/3 degree latitude by 1/4 degree longitude), with 10 (version M10) or 16 (version EE16) vertical levels. All experiments are initialized by NMC Hemispheric Analysis valid for 0000 UTC 04 JAN 1989. This series incorporates non-divergent winds on pressure surfaces and observed temperatures. Boundary values are nudged towards the 12 hour NMC analysis using:

$$\left(\frac{\partial X}{\partial t}\right) = (1-\alpha)\left(\frac{\partial X}{\partial t}\right)_m + \gamma (X_o - X)$$

where X is a dependent variable, subscript 'm' denotes the model tendency, τ is a relaxation parameter, and X_o represents the large scale (initialization field) value. Besides the cumulus parameterization scheme already discussed, parameterized processes include convective precipitation, dry convective adjustment, and Planetary Boundary layer (PBL) mixing (Holt et al., 1990).

Two versions of the model are used in this experiment series. The degraded M10 model provides the reference atmosphere. The bottom layer encloses the PBL, parameterized by the bulk aerodynamic (drag coefficient) method. Sea surface temperatures are from January climatology on a 1° resolution grid (Reynolds, 1982). The sixteen layer EE16 version of the model generates the simulated SSM/I observations. EE16 models the PBL using turbulent kinetic energy (TKE) closure theory, incorporating prognostic equations for turbulent kinetic energy transport and dissipation. TKE is derived as a function of shear production, buoyancy production and turbulent transport. The

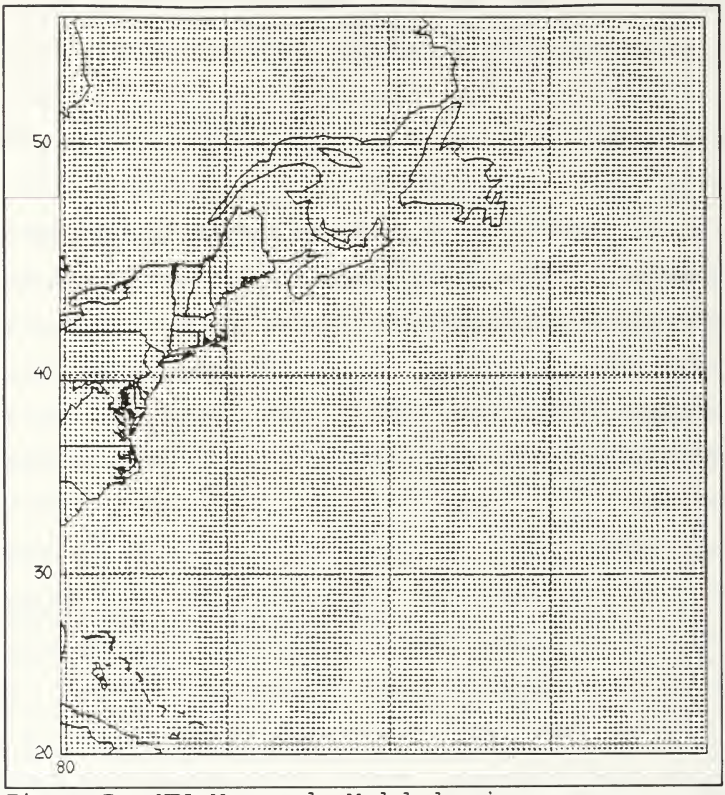

Figure 7. NRL Mesoscale Model domain.

surface energy balance is maintained via the soil slab model (Chang, 1979). Dissipation of the energy results from imbalances in production, destruction and transport (Holt et al., 1990).

Tests of M10 involve the assimilation of moisture and wind fields from EE16. Varying adjustments of assimilation time, spatial domain (simulating satellite swath widths) and the vertical distribution method for moisture comprise the sensitivity tests, described in the next chapter.

IV. OBSERVING SYSTEM SIMULATION EXPERIMENT (OSSE) DESIGN

A. COMPARISONS OF SSM/I IMAGES AND 16 LAYER MODEL OUTPUT

Before proceeding with the OSSE, EE16 must be shown to reasonably simulate SSM/I data. Comparison of model output from EE16, the full physics model, with SSM/I observations indicates that EE16 can serve as the simulated observation system in the OSSE. While EE16 does not perfectly reproduce the SSM/I product it does produce storm depictions with two useful features. The model output is a good approximation to the satellite image when considering storm structure and intensity compared to observations. Position and magnitude comparisons of post-storm analysis, satellite images and model outputs support these findings.

1. Satellite Data

Using NRL algorithms and NPS IDEA Lab systems, images of SSM/I surface wind speeds and water vapor (total precipitable water) are created. SSM/I passes over the domain are available for 0000 UTC, 0930 UTC and 2200 UTC as shown in Figures 4, 5, and 6. With land masking applied to the images, the highest concentrations of water vapor, rainfall intensity and surface wind maxima are tracked for location, intensity and translation speed analysis. These are compared to

simulations from the 16-layer NRL model with a modified cumulus parameterization scheme.

2. Wind Speed

SSM/I surface wind speed for 0000 UTC, 0930 UTC and 2200 UTC 4 JAN 1989 are shown in Figures 8, 9 and 10 respectively. Unfortunately, most of the wind speed maxima indicated in these images are collocated with heavy rain cells, reducing the accuracy to within 5 m/s as indicated in Figures 4 through 6. In Figures 9 and 10, the wind maxima are at the western edge of the swath. In truth, the storm center was further west, out of the area of SSM/I coverage. The 0930 image is straddled temporally by EE16 plots at 0600 UTC and 1200 UTC, which depict a circular high wind speed area propagating northeastward (Figures 11 and 12). Rainfall near the center of this system makes SSM/I magnitudes unreliable, but towards the outer edges of the storm there is agreement in the contours of 6 to 24 m/s winds. EE16 generated wind fields at 1800 UTC and 2400 UTC (Figures 13 and 14) show the same comma pattern exhibited in the SSM/I image. (Throughout the analysis, '2400 UTC' will refer to the ending time of the experiment trials. The actual calendar time would be 0000 UTC 5 January 1989.) In both model generated plots, the actual storm center and associated wind speed maximum lay to the west of the comma structure, just outside the satellite swath.

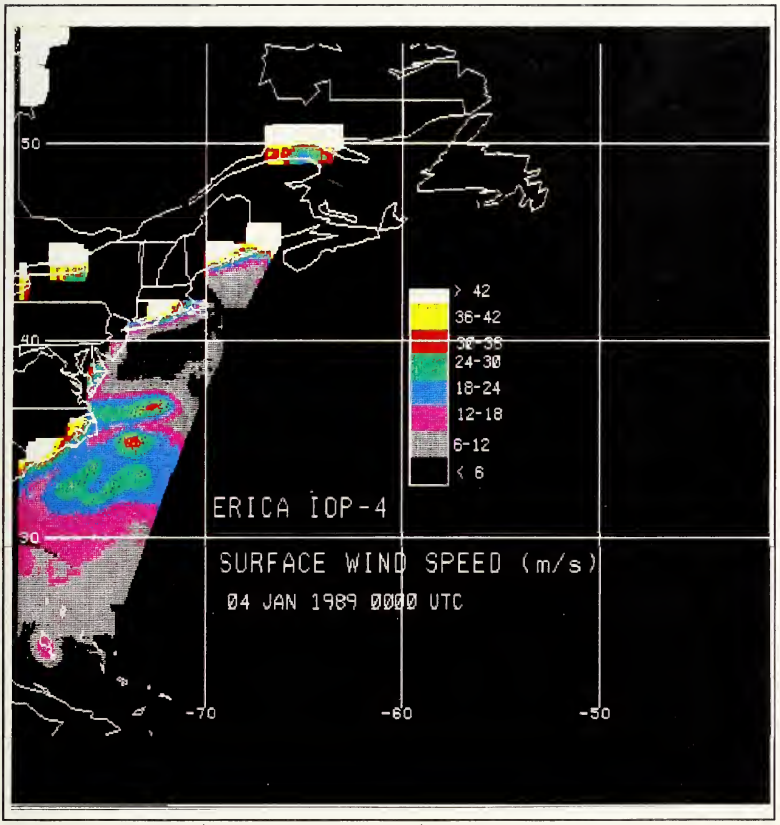

Figure 8. SSM/I wind speed (m/s) at 0000 UTC.

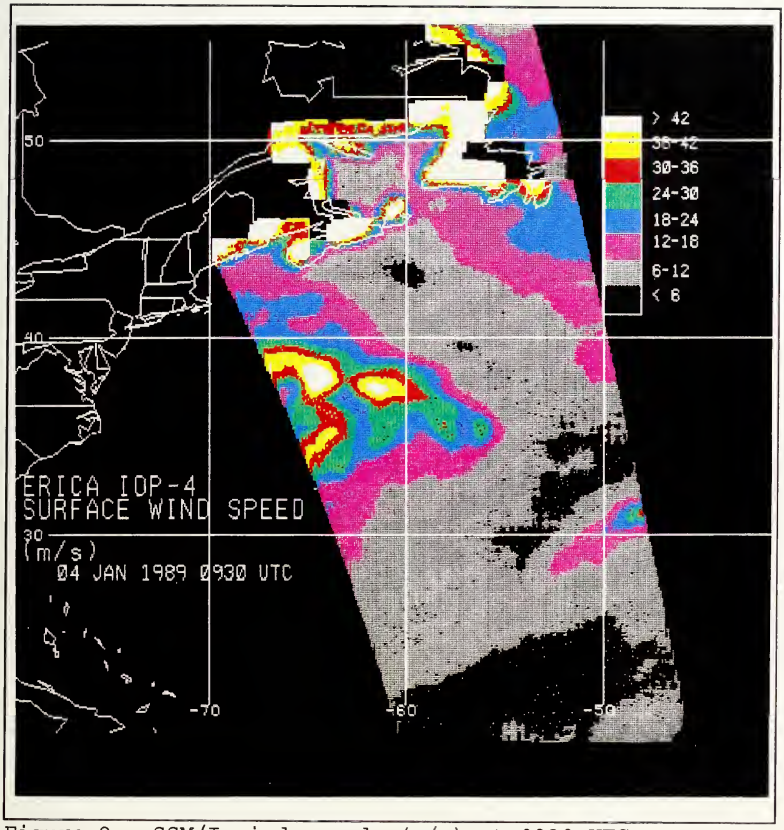

Figure 9. SSM/I wind speed (m/s) at 0930 UTC.

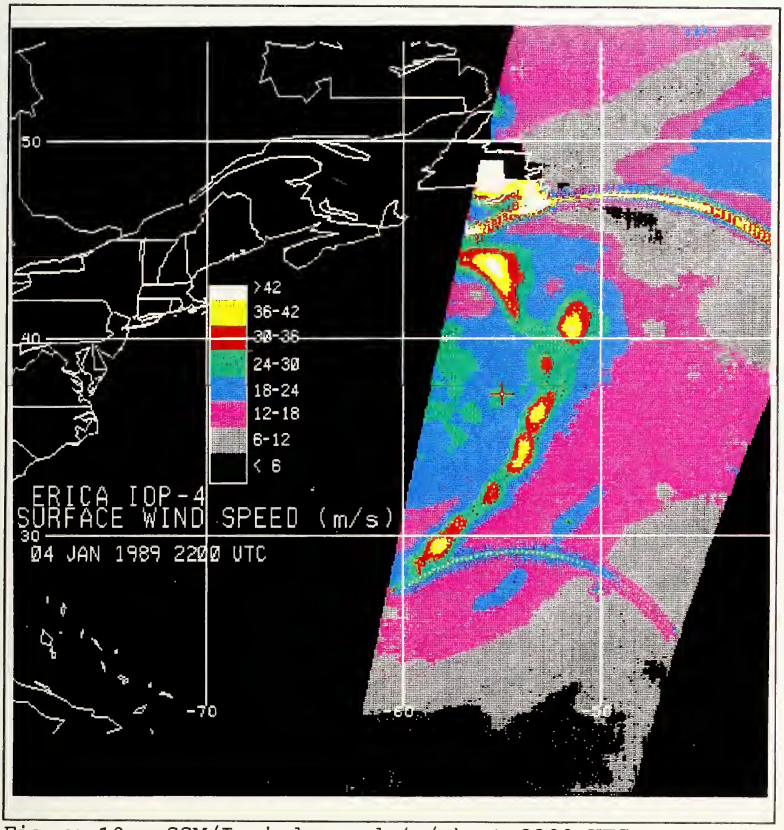

Figure 10. SSM/I wind speed (m/s) at 2200 UTC.

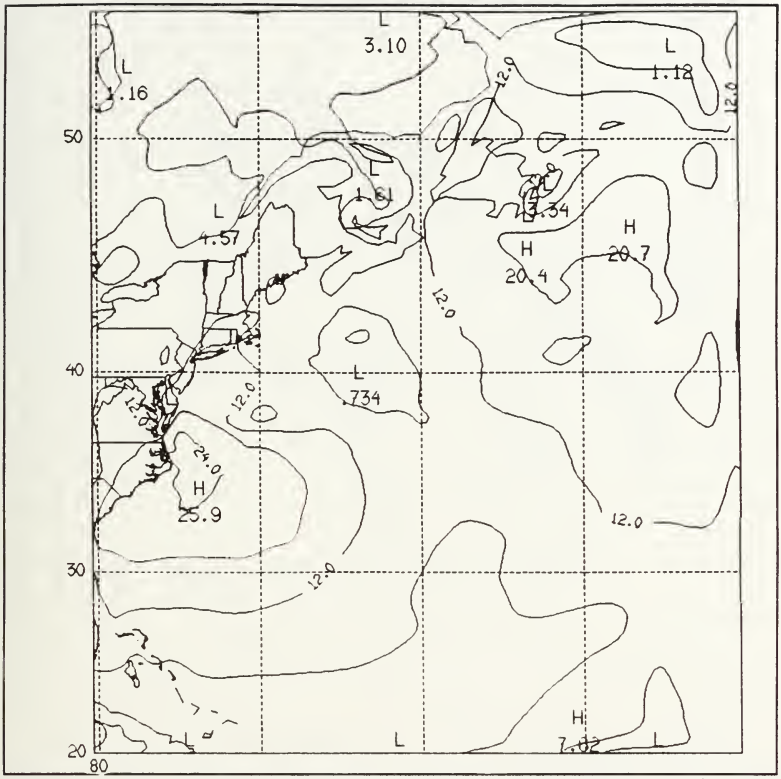

Figure 11. EE16 generated surface wind field (m/s) at 0600 UTC.

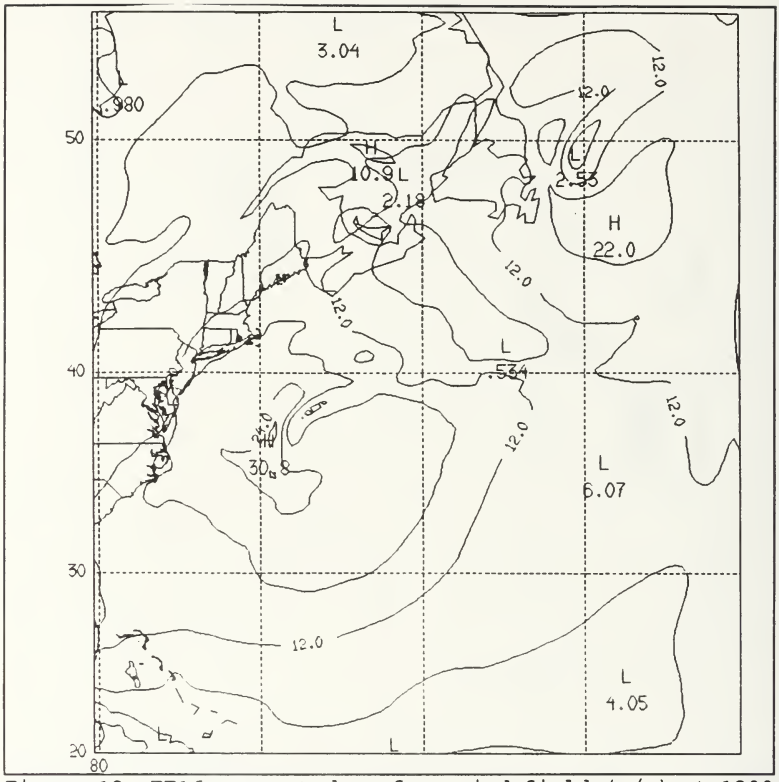

Figure 12. EE16 generated surface wind field (m/s) at 1200 UTC.

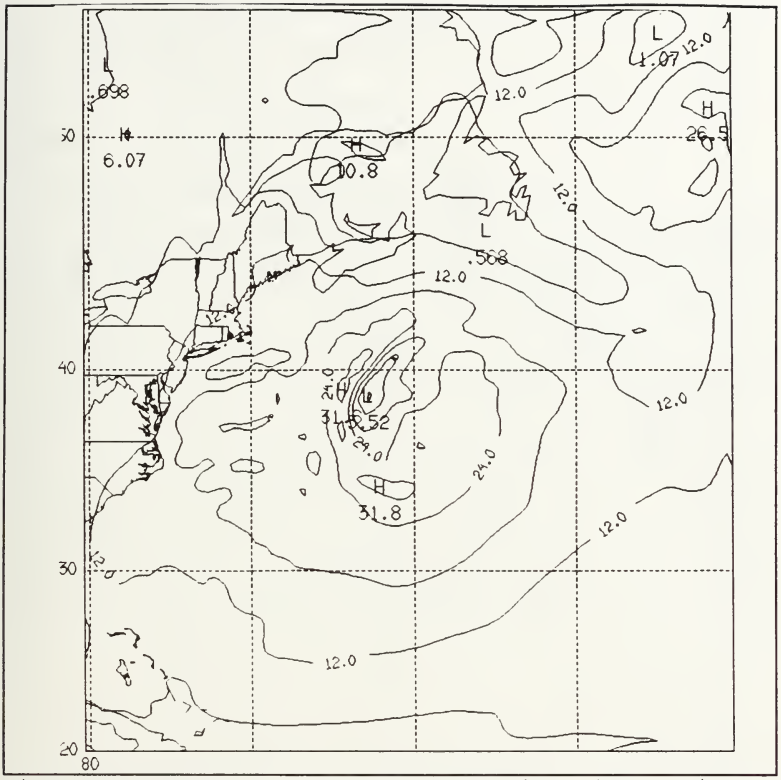

Figure 13. EE16 generated surface wind field (m/s) at 1800 UTC.

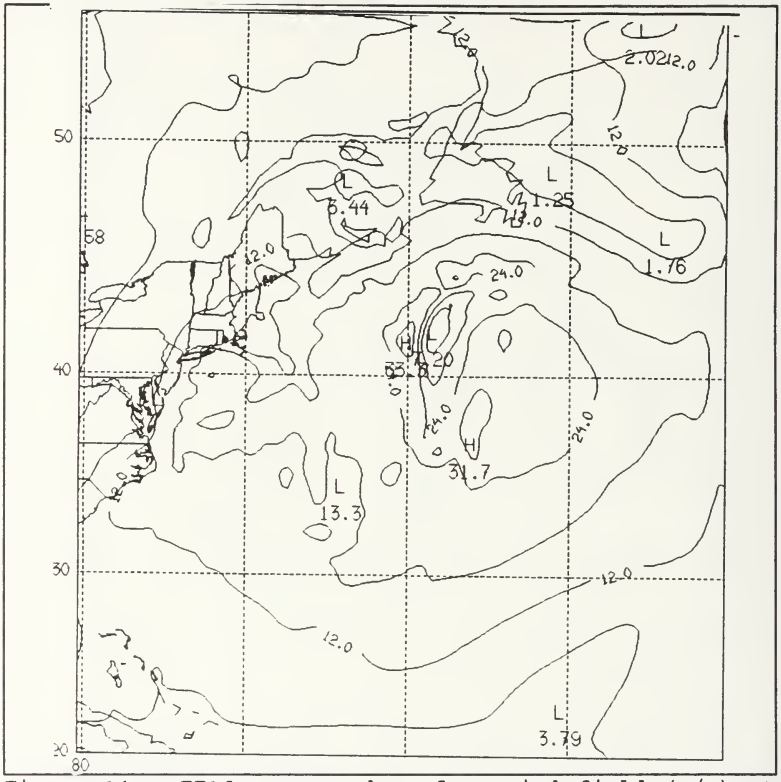

Figure 14. EE16 generated surface wind field (m/s) at 2400 UTC.

Note the wind speed minimum evident at the extreme western swath edge near the comma head in the SSM/I image shown in Figure 10. This corresponds to a model indicated minimum eastward of the comma structure.

3. Water Vapor (Total Precipitable Water)

SSM/I water vapor images and total precipitable water plots generated by EE16 support the use of EE16 as a simulated observational system. The terms 'water vapor' and 'total precipitable water' may be used interchangeably in this case. Figures 15, 16 and 17 are SSM/I images of water vapor for 0000, 0930 and 2200 UTC respectively. Figures 18 through 21 show that EE16 produces a structure very similar to the SSM/I images regarding total precipitable water distribution. Evolution of the circular precipitable water center defined by the 30 -36 kg/m^2 contour in Figure 16 to the banded, T-bone structure defined by the same contour in Figure 17 compares favorably with the EE16 series. In Figure 18, EE16 produces a circular 36 kg/m^2 precipitable water area centered near 32° N, 70° W evolving to a T-bone structure defined by the 30 kg/m^2 contour in Figure 21.

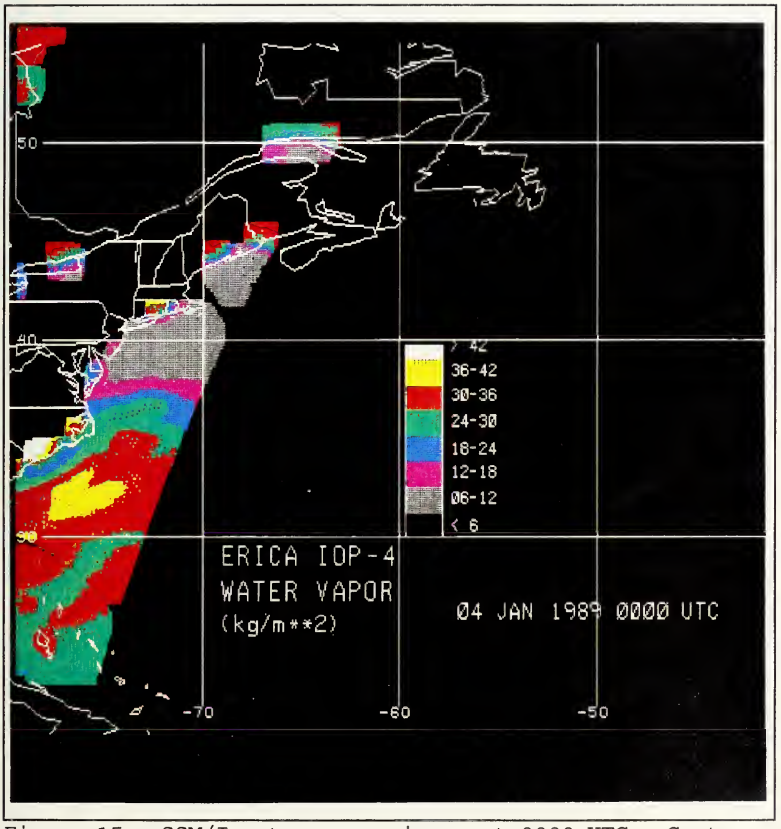

Figure 15. SSM/I water vapor image at 0000 UTC. Contours depict precipitable water amounts in kg/m^2.

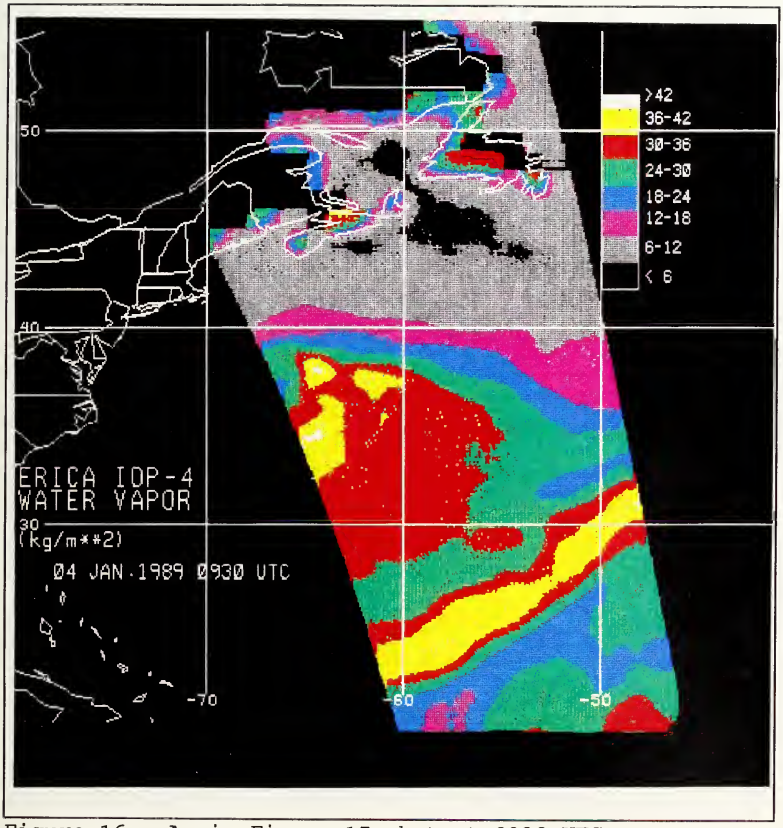

Figure 16. As in Figure 15, but at 0930 UTC.

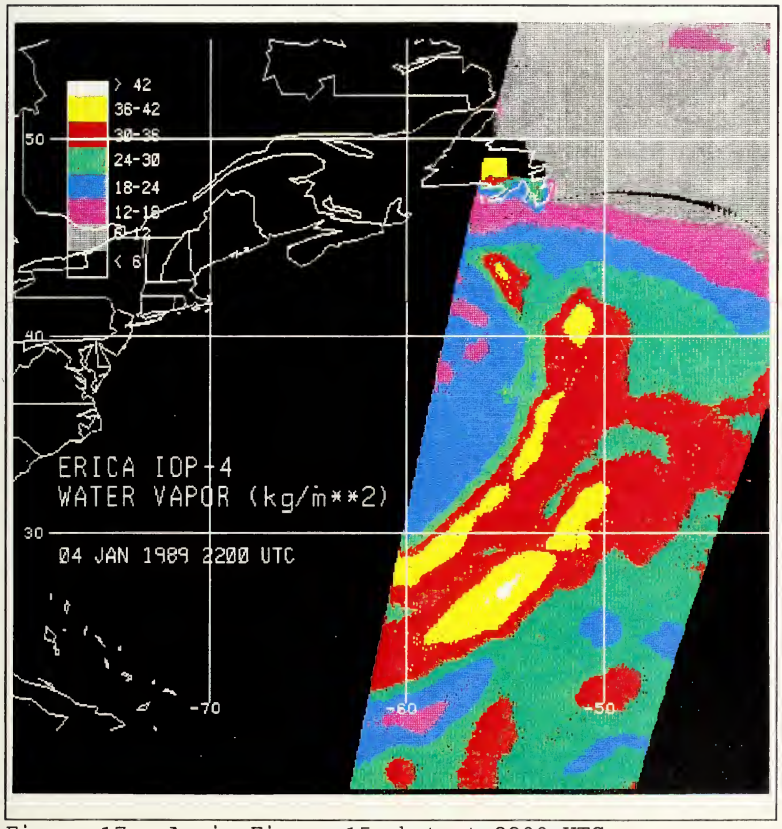

Figure 17. As in Figure 15, but at 2200 UTC.

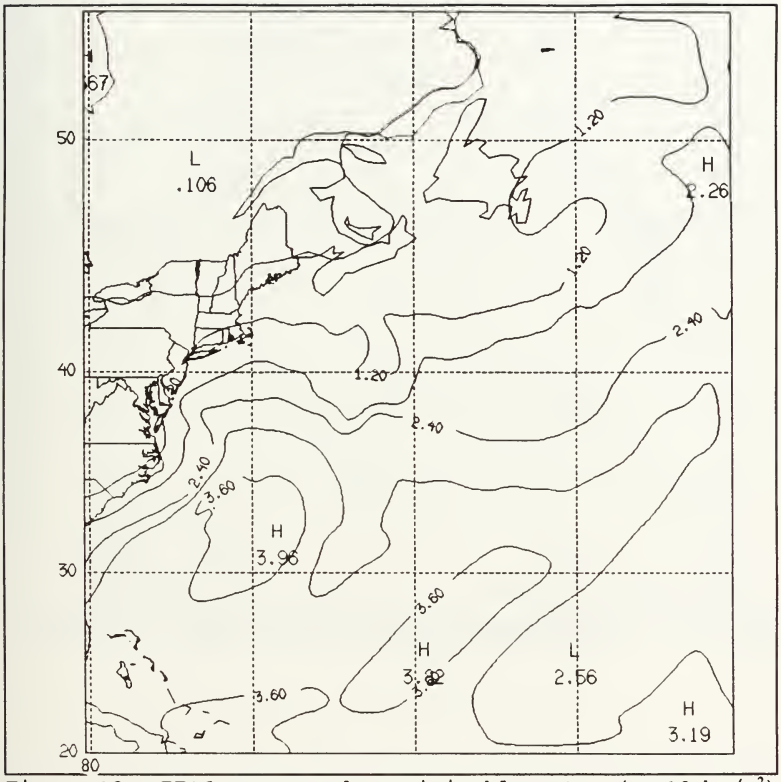

Figure 18. EE16-generated precipitable water (x 10 kg/m^2) at 0600 UTC.

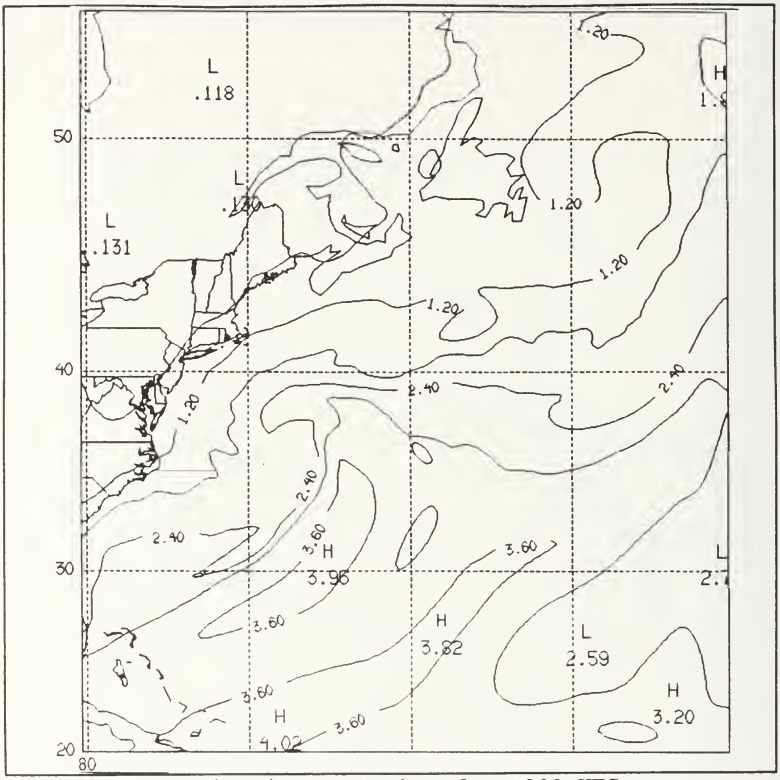

Figure 19. As in Figure 18, but for 1200 UTC.

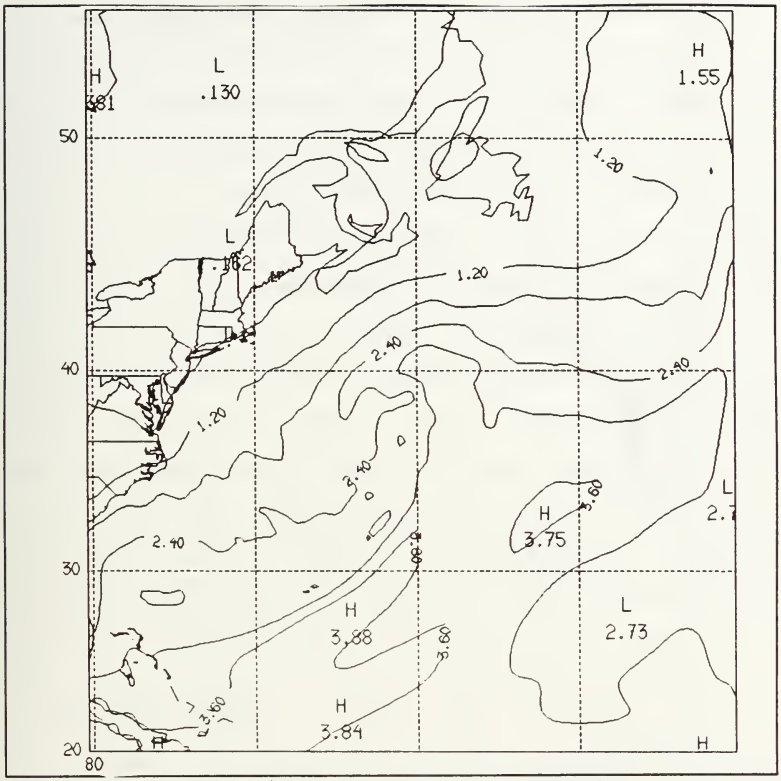

Figure 20. As in Figure 18, but at 1800 UTC.

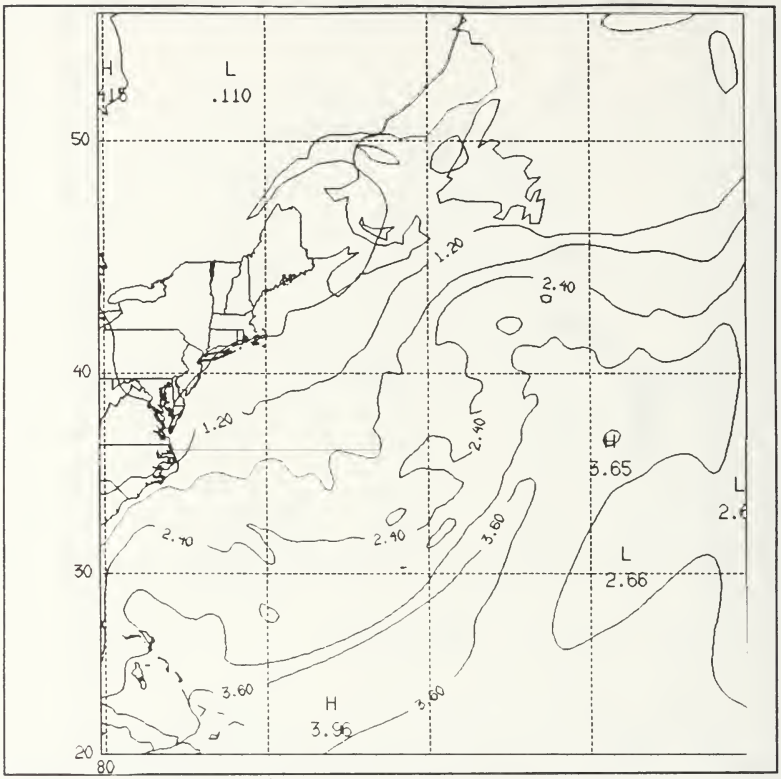

Figure 21. As in Figure 18, but at 2400 UTC.

Magnitudes of total precipitable water do not support use of EE16 as an observation simulator, but the trend in development makes them suitable. Since the actual storm deepened to 936 mb by 2400 UTC while the 16 layer model goes only to 956, it is not expected that all parameters show agreement. The SSM/I, with an error of 2.4 kg/m^2, indicates an initial rise in water vapor followed by a leveling at 45 kg/m^2. The sixteen layer model agrees with this rise in precipitable water amounts. Again, these SSM/I values are amplified due to the removal of the precipitation screen. Since this storm deepened much more than the 16 layer model predicts, the SSM/I values are assumed to be much closer to the truth. However, EE16 does duplicate the trend and approximate the magnitude, and will be accepted as an observing system simulator.

B. EXPERIMENT DESIGN

1. OSSE

To observe the impact of satellite data on the NRL model forecast, an Observing Systems Simulation Experiment (OSSE) is conducted. This OSSE is specifically organized to contrast dynamic and diabatic forcing variables. The experiment series structure follows the Air Force Geophysics Laboratory description of a "Fraternal Twin" OSSE (Lipton, 1989). The reference atmosphere will be generated by allowing a degraded version of the NRL 10-layer model (M10) to run over

the 24 hour observation period. Degradation of the model results in a greater separation in skill level of the two systems being run. In these tests, M10 is hindered by an imposed 50% underestimation of horizontal water vapor convergence in the Kuo convective parameterization scheme. Diffusion is amplified by a factor of four. This inhibits latent heat release and, consequently, storm deepening. Simulated observations will be generated by the more complex 16-layer model (EE16) with full model physics. This version models the planetary boundary layer with seven vertical levels, compared to M10's bulk PBL parameterization contained in the single lowest level. These simulated observations will consist of atmospheric moisture content and surface wind speed.

To conduct the OSSE, these simulated observations are then incorporated into the 10 layer model reference atmosphere in the various schemes summarized in Table 3. Each column presents a feature of the experiment. Test names start with "T" for assimilation of a variable over the entire domain or "S" for assimilation only over the areas of satellite coverage (swaths). The second letter identifies the tested parameter, as "W" for surface winds, "M" for substitution of the 16 layer moisture into the 10 layer model, or "V" for vertical distribution of the moisture correction suggested by the 16 layer model. Column 2 indicates the number of "observation" updates made during the experiment. Column 3 states the

amount of time each "observation " was held valid. The "Lead" column defines the amount of forward lead time allowed in the incorporation of 16 layer data. (For example, the 0600 UTC EE16 winds are used by M10 at run time 0300 for a lead of 3 hours.)

TABLE 3. SUMMARY OF EXPERIMENTS

Test	Observations	Period	Area	Lead	Ending Pressure
TW1	4 (Surface Wind)	6 Hours	Domain	None	966 mb
SW1	4 (Surface Wind)	6 Hours	Swath	None	969 mb
TV2	4 (Vertical Moisture)	6 Hours	Domain	6 Hours	974 mb
TM2	4 (Moisture)	6 Hours	Domain	6 Hours	968 mb
SM2	4 (Moisture)	6 Hours	Swath	6 Hours	973 mb
TV3	4 (Vertical Moisture)	6 Hours	Domain	3 Hours	973 mb
TW4	2 (Surface Wind)	12 Hours	Domain	6 Hours	967 mb
TM4	2 (Moisture)	12 Hours	Domain	6 Hours	973 mb
TV4	2 (Vertical Moisture)	12 Hours	Domain	6 Hours	973 mb

2. Analysis plan

Various sensitivity tests will be run using combinations of simulated satellite parameters. Although the

SSM/I provides only directionless wind speed, since these speeds are successfully modeled it will be assumed that the model generated wind directions are also valid. Another induced artificiality is the vertical distribution of water vapor. Since the SSM/I provides a single value for water vapor representing the contents of the atmospheric column above a point at the surface, a method of numerically distributing this water throughout the column is required. Section D contains a description of the vertical distribution scheme employed by the 10 layer model.

Following collection of NCAR-Graphics generated plots of various fields for each model run, development of the storm will be examined to assess the relative importance of wind speed and the horizontal and vertical distribution of water vapor. Besides the storm features described by other studies in the previous section, analysis of the model runs will focus on the meteorological processes listed below.

Vertical storm development will be examined with respect to the increase of circulation intensity with height and interactions with short waves. Wind structure, pressure and temperature contours will be used to determine the character of the flow and the structure of the storm.

Of particular interest in this study is the structure and function of moisture distribution within the storm. Diurnal effects of moisture transport will be observed; however, conclusions will be limited since this is a single

24-hour period under discussion. Cross sectional analysis will describe vertical motion fields in the vicinity of fronts.

Four series of sensitivity tests are performed on the ten layer model (M10) to determine the most critical parameters in describing the behavior of a rapidly deepening cyclone. Each series of tests contains up to three variations on variables used and spatial domain included. The first series updates the M10 fields with coinciding fields from EE16 every six hours. Series II initializes the M10 run with selected fields from the 0600 UTC EE16 run, and continues to update every six hours. Series III resembles the first series, with the update times moved three hours earlier. Finally, Series IV suggests the pattern obtained if updates were received from a polar orbiting satellite, using two updates spaced twelve hours apart. Figure 22 is a line diagram illustrating the flow of the tests. These tests provide information on which parameters M10 is most sensitive to in explosive cyclone prediction, but they do not represent operationally usable methods since 'a priori' knowledge of the atmosphere is assumed in most of the runs.

C. SERIES I: COINCIDENTAL FOUR PERIOD NUDGING

In the first experiment series, M10 marches through time normally with respect to all the state variables except the u and v surface wind component fields. These fields are nudged

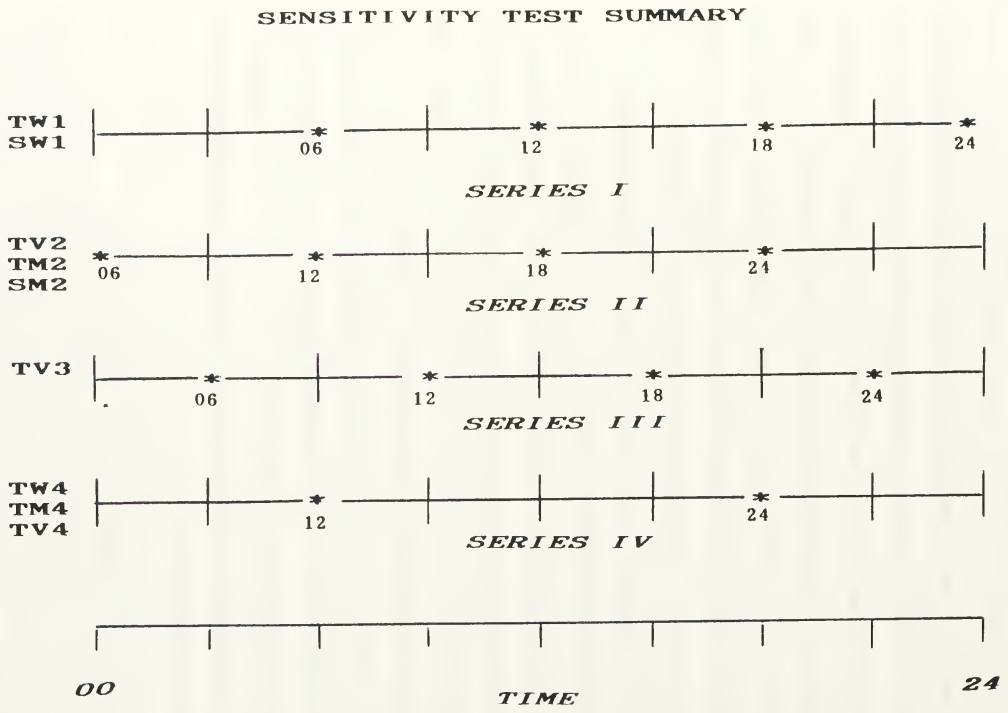

Figure 22. Sensitivity test summary. Asterisks indicate update points using EE16 data. Numbers below asterisks indicate generation time of update information by EE16.

towards their respective EE16-generated values at 0600 UTC during the first six hours of the model run, toward the 1200 UTC value during the second six hours, the 1800 UTC fields during the third four hour period, and towards the 2400 UTC values for the final four hours of the test. This series includes two runs, TW1 and SW1. In TW1, winds are nudged over the entire spatial domain of the case study, while SW1 nudges the winds only over the SSM/I swaths covering the ERICA area.

The primary step in the nudging process involves converting the 16 layer wind into a compatible 10-layer product from which a surface value can be extracted. The subroutine MWWIND in the NRL Model applies a mass-weighting function to the 16 layer vertical wind profile. Figure 23 illustrates this vertical weighting function. The lowest seven layers of the weighted profile are averaged and extracted as the "Observed" surface wind. Once this value has been obtained, standard Newtonian nudging practices are followed to gradually update the M10 winds. In practice, the new M10 wind depends on the horizontal pressure gradient, coriolis parameter and "observed" wind.

For SW1, the model defines the slope of the swath boundaries. At the same times as in run TW1, winds over the swath region are nudged to coincident EE16 values. Estimation to the actual swaths are made, using the 0000 UTC swath for model nudging from 0000 to 0600, the 0930 swath for data

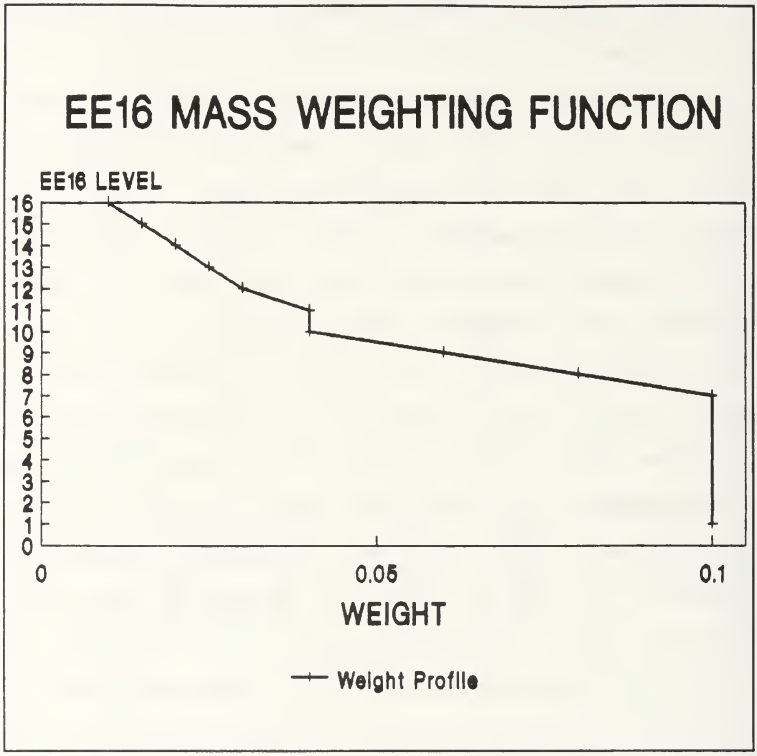

Figure 23. Vertical weighting function for conversion of 16 Layer data to 10 Layers.

between 0600 and 1200 and the 2200 swath for requirements after 1800.

D. SERIES II: MOISTURE ASSIGNMENT AND DISTRIBUTION

The second series of experiments diagrammed in Figure 22 begins with assignment of the 0600 EE16 moisture ("q" values) to the 0000 UTC M10 atmosphere. The model runs until 0600 when the 1200 EE16 moisture is similarly assigned. This six hour lead repeats until the end of the experiment. Both a total domain test (TM2) and swath assignment test (SM2) are performed.

Series II also includes a procedure for distributing the total precipitable water "observed" over the vertical 10 layer column (TV2). The NRL Model subroutine QDISTNRL performs the vertical moisture distribution adjustment at those grid points indicating a significant difference between M10 and EE16 derived total integrated water content. This correction can be negative to indicate drying of the column, or positive for moistening. At these points, vertical levels in the 10 layer model are examined to determine unsaturated layers which could absorb portions of a positive (adding moisture) correction, using subroutine ESAT to provide the specific humidity profile at the grid point. The M10 value for humidity in the column is then adjusted by the following:

$$q(K)_{NEW} = q(K)_{OLD} + CORR * \left(\frac{relh(K)}{relh_{\Sigma_{unsat}}} \right)$$

Where $q(K)_{new}$ represents the new moisture value in a given layer, CORR the total correction applied based on the EE16-M10 moisture difference, RELH the relative humidity, and $RELH_{\Sigma\ unsat}$ the relative humidity in the unsaturated layers. After the vertical moisture redistribution, control checks insure no layer has been supersaturated or "hyper-dried". If such has occurred, humidity profiles are recomputed using the adjustment scheme until no supersaturated or "hyper-dried" regions exist.

E. REMAINING SERIES

1. Centered Four-Period Assignments

Series III consists of a single vertical distribution run, TV3, using the algorithm described in QDISTNRL. Here, M10 runs normally until 0300 when the integrated water content computed by EE16 at 0600 is inserted. M10 runs from this assignment until 0900, reacting to the redistribution. Using this scheme, the observation is centered within the assimilation period (i.e., the 0600 observation is centered between 0300 and 0900). Three periods of six hour run times follow, centering the 1200, 1800 and 2400 EE16 integrated water content observations as shown in Figure 22.

2. "Polar Orbiter" Simulator

Series IV contains three runs over the entire domain, testing winds (TW4), surface moisture (TM4) and vertical distribution moisture adjustment (TV4) when "updated" twice at a twelve hour interval as opposed to the six hour updates of the previous tests. A centering scheme is used again, as M10 is assigned the 1200 UTC EE16 value at model time 0600 UTC, and assigned the 2400 UTC EE16 value at 1800 UTC, allowing the model to run normally for the final six hours.

F. FINAL COMMENTS

The experiments described in this chapter are not operationally feasible since most require assimilation of "future" data which would not be available to an operational model. They can, however, provide insight toward the trend of corrections needed to improve the model performance for a given type of storm. In the next chapter, these sensitivity test will show the vulnerable areas of M10 in modeling explosive extratropical cyclones.

V. ANALYSIS OF RESULTS

A. OVERVIEW

ERICA IOP-4 exemplifies a dynamically-driven storm with diabatic processes playing a secondary role in the development of the storm. The assimilation of wind speed data has the greatest effect on model performance. Model depiction of cyclone circulation interacting with the environmental flow impacts the development rate of the storm. Secondary deepening effects are revealed in precipitation amounts and areal coverage which imply the degree of latent heat release. Although no experiment deepens the storm to the analyzed 936 mb intensity, or even to the 956 mb low predicted by the EE16 run, significant improvements from the 971 mb degraded run are observed with wind speed inputs. Greater deepening rates with better defined frontal structures are gained from wind speed inputs. Sensitivity to moisture distribution is also demonstrated.

B. COMPARISON OF SENSITIVITY TEST RESULTS

Four areas of study arise from the sensitivity tests described in Figure 22. First; although modelers acknowledge the value of accurately initialized winds in a numerical prediction scheme, these values are not often readily available. Sensitivity test Series I (TW1 vs. SW1) examines

the degree of improvement afforded by incorporating the winds over the satellite swath compared to the improvement gained by incorporating winds over the entire domain. Second, sensitivity test Series II provides two comparisons to determine the most productive use of satellite obtained moisture. Within this series, a comparison of swath vs. domain surface "q" values is performed similar to the first wind test. Additionally, the series tests the value of vertically distributing the "observed" moisture throughout the atmospheric column in a domain test.

Test Series III, consisting of one vertically distributed moisture test, compares to the vertical test from Series II giving an indication of the model sensitivity to assimilation time difference. This comparison investigates the value of reducing the six hour lead time to three hours as well as a "centered" estimation time versus a "lead" time. For the final comparison, Series IV places surface winds, surface moisture and vertically distributed moisture in identical update situations to determine the most effective of the three parameters for explosive cyclone modeling.

C. SERIES I: SWATH VS. DOMAIN WIND ASSIMILATION

Storm development is traced for the first series of experiments in Figure 24. Significant differences in wind speed structure develop at 1200 UTC. At the surface in the

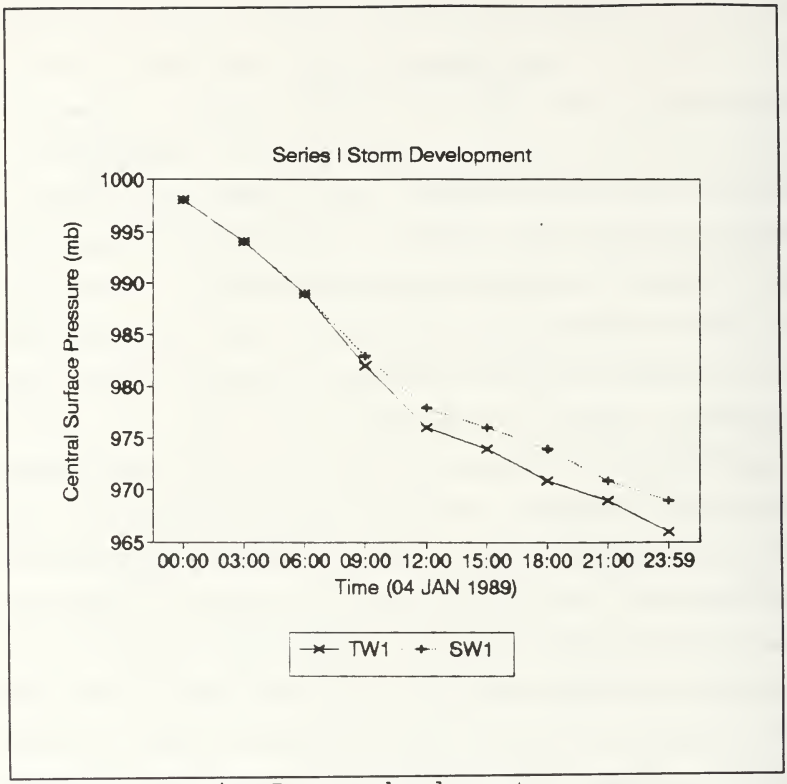

Figure 24. Series I storm development.

immediate vicinity of the storm (directly east of the DELMARVA peninsula at 38° N, 64° W), TW1 models a strong zonal wind speed gradient, shown in Figure 25. At the same time, SW1 displays more curvature as the local wind speed high of 32.2 m/s has already swung to the southeast of the wind speed minimum. Winds above 500 mb show little change and do not appear to be sensitive to the surface wind distribution this early in the test.

The experiments in Series I provided the best storm development in terms of surface pressure deepening. Both runs have a significant impact upon the surface momentum field. Figure 26 presents surface and temperature fields at 2400 UTC. With swath wind inputs from 2400 UTC applied, SW1 only lags TW1 by 3 mb in storm development. SW1's ability to remain close to TW1 in storm development is largely attributable to the early swaths coinciding with the areas of most intense storm development. Although TW1 surface pressure remained consistently deeper than SW1, the latter displays more distinct frontal structure. Since the first satellite pass covers the area of storm development, the cyclone is highlighted by the model in SW1. The two experiments produce wind fields with differing orientations. Figure 27 displays the surface isotach field for each run at 2400 UTC. TW1 places local maxima of 34.5 m/s and 35.0 m/s north and south, respectively, of the local minimum. SW1 positions local

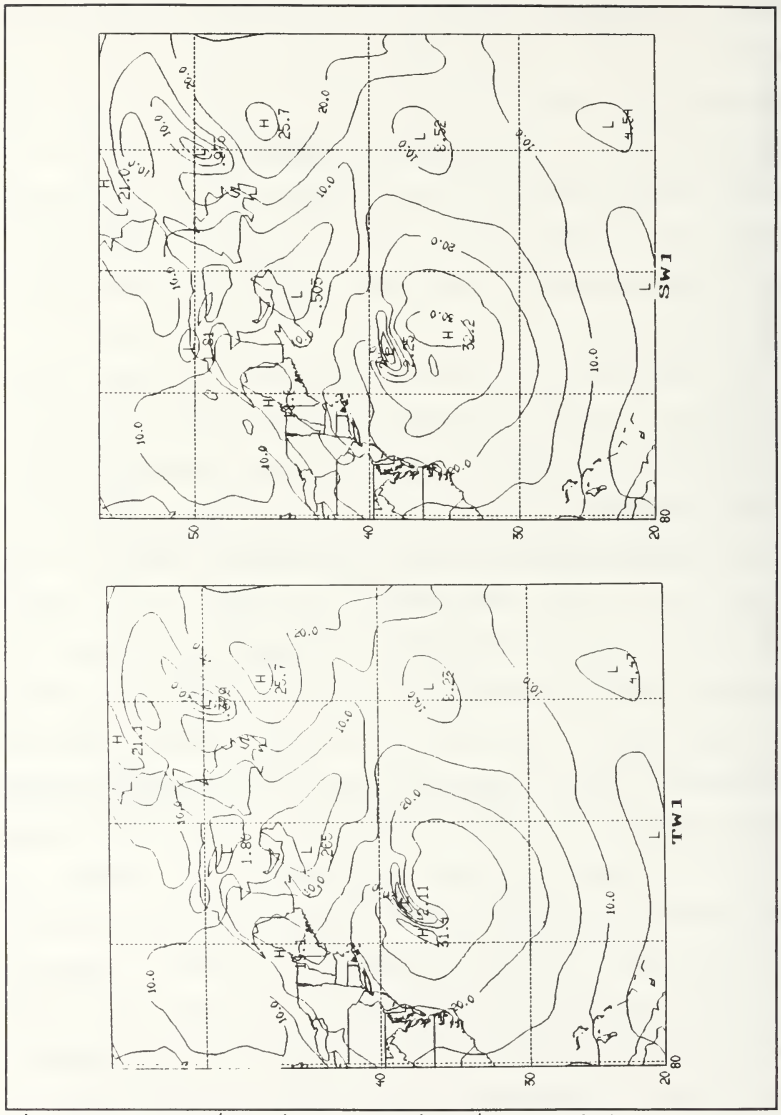

Figure 25. TW1/SW1 isotachs, in m/s, at 1200 UTC.

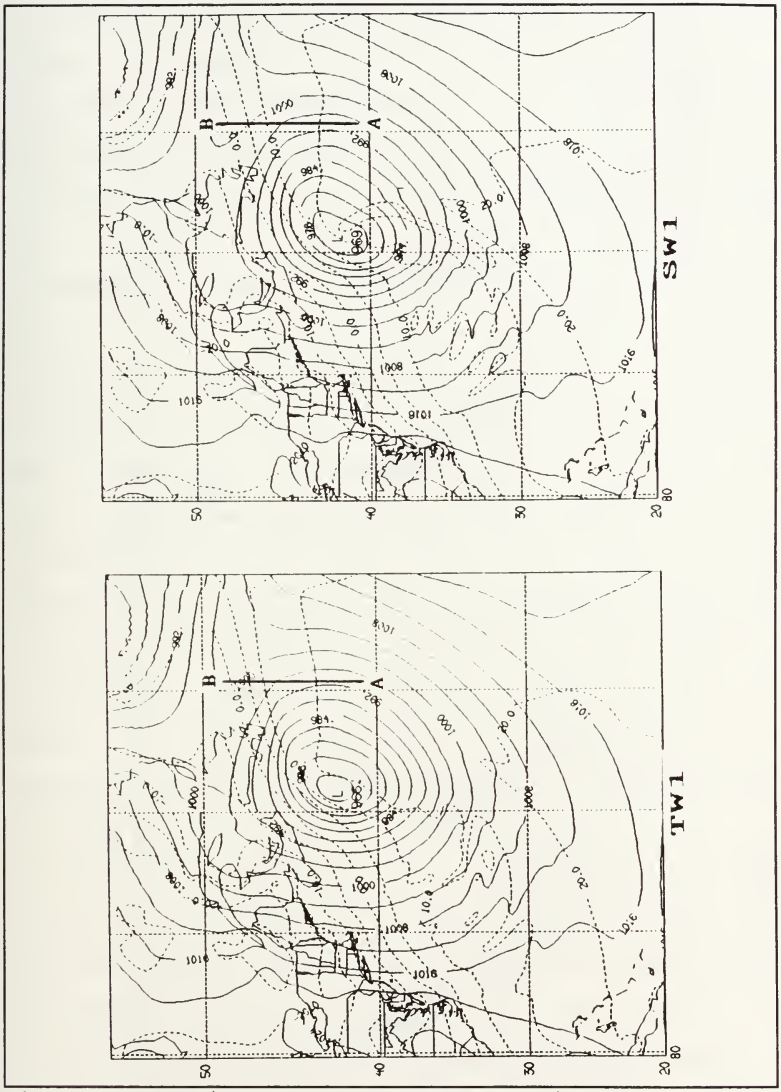

Figure 26. TW1/SW1 surface pressure (solid lines, mb) and temperature (dashed, °C) at 2400 UTC.

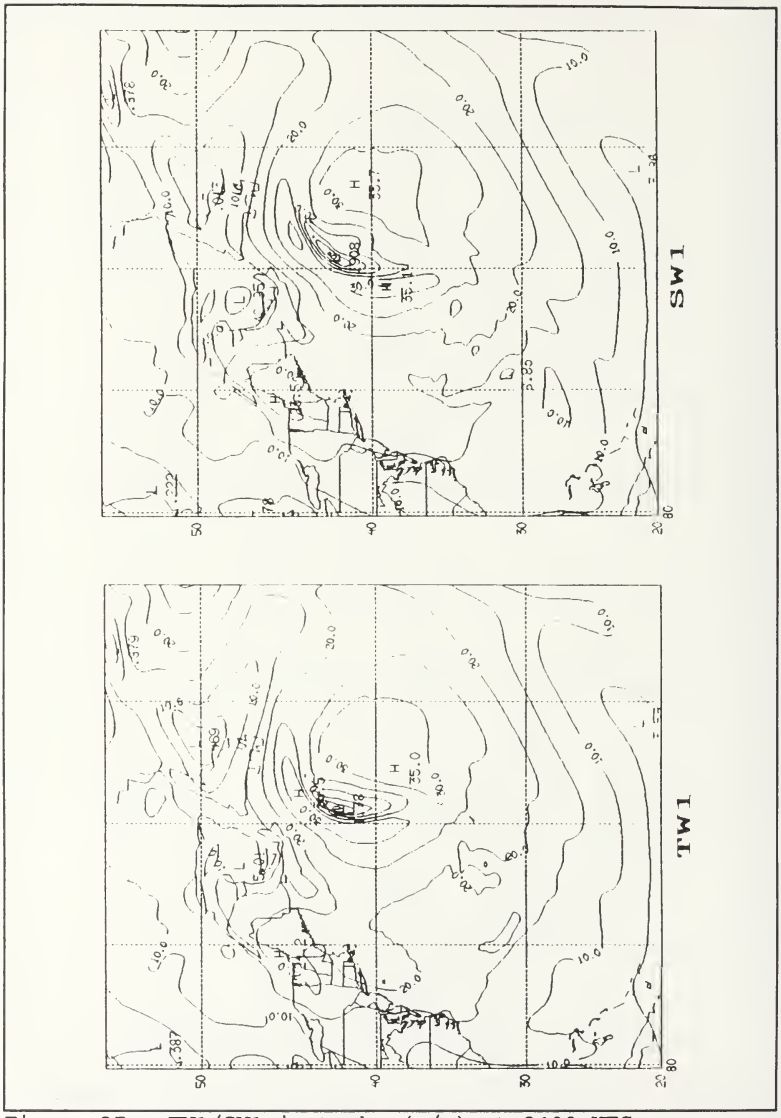

Figure 27. TW1/SW1 isotachs (m/s) at 2400 UTC.

maxima of 35.1 m/s (east) and 33.7 m/s (west) around the local minimum. Comparison of precipitation areal coverage and amount shows small differences related to LHR and upward motion between the two experiments. Although a specific study of heating rate assimilations is to be done in a future paper, impact of differing heating rates is evident in these experiments. The improved deepening rate of TW1 can be traced back to the 1200 UTC cross sections through the warm front. In Figure 28, on the southern edge of the warm front the omega field shows upward motion and tighter omega gradients to higher levels than the SW1 plots shown in Figure 29. The tighter gradient feature continues through 2400 UTC, ending up farther north in TW1 than SW1. Across the cold front, which is better represented in SW1 due to the contrast in resolution inside and outside the swath, rising motion in the warm sector at 1200 UTC is distinct in SW1 and minimal in TW1. This contrast does not maintain itself past 1500 UTC, as the subsequent satellite pass misses portions of the storm as the low center moves eastward.

Statistical analysis is performed to check the performance of the model and the impact of the experiment variations on a grid scale over the entire domain. Statistical plots used in this analysis consist of root-mean-square (RMS) errors and S1 scores computed against the corresponding EE16 fields. In Series I, Figure 30 shows surface wind RMS errors are initially larger for TW1 than for SW1. By the end of the run,

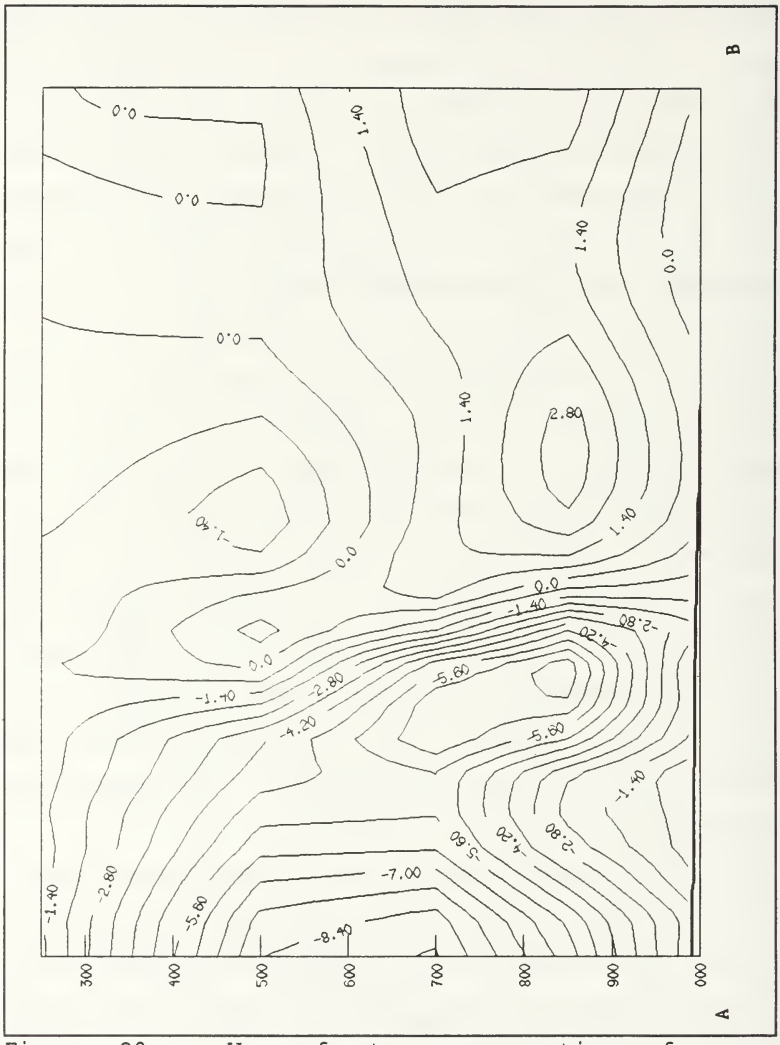

Figure 28. Warm front cross section of omega (microbars/sec) for TW1 at 2400. "A" and "B" correspond to points on Figure 26.

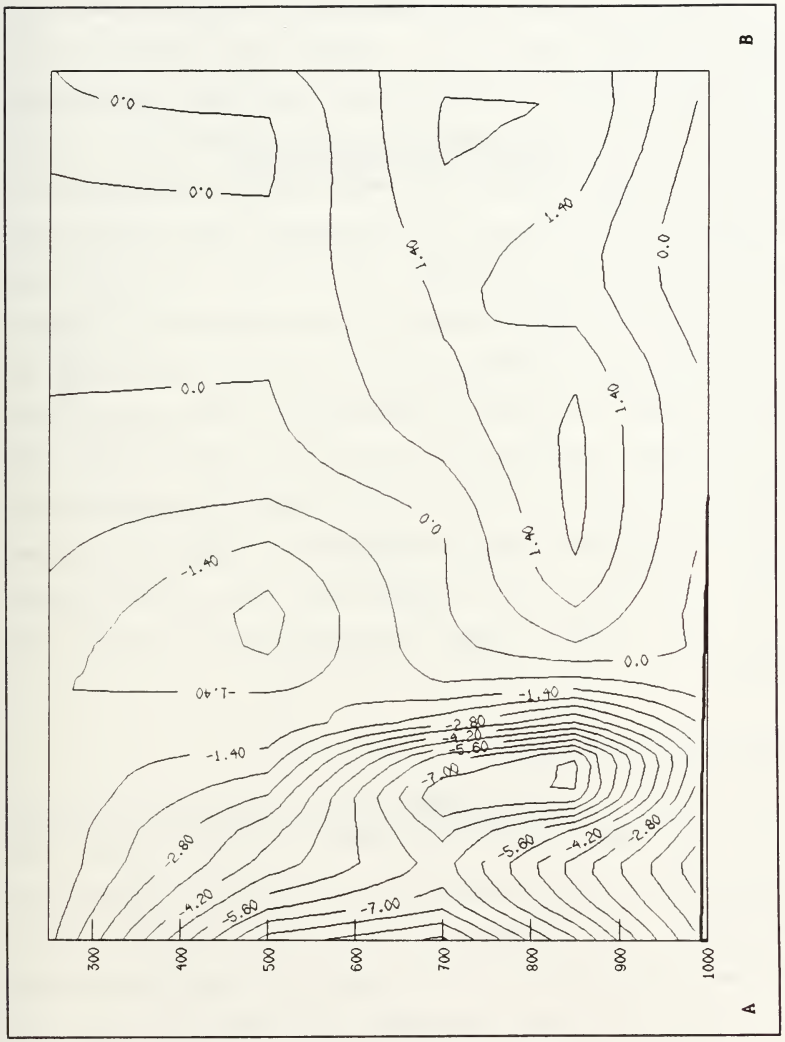

Figure 29. As in Figure 28, but for SW1.

it is evident that TW1 has maintained an overall lower error compared to the EE16 run. During the course of the experiment, the swath passes used in SW1 get progressively farther from the storm center and the highest winds. By the end of the experiment, the swath update information is correcting low magnitude wind differences while leaving the major discrepancies untreated. At 850 mb, both runs have similar RMS wind errors indicating the relatively low impact the domain-swath variation has on vertical wind structure. Finally, Figure 31 shows the comparison of storm tracks based on low pressure centers generated by the two experiments. SW1 follows the same track as TW1 but at a slightly reduced speed. Again, this is swath location dependent as the earlier updates improve the storm center information, while later updates outside the cyclone reduce the environmental wind speed gradient.

D. MOISTURE SENSITIVITY

1. Domain vs. Swath Comparison

From Table 3 in Chapter IV it is clear that incorporation of surface moisture over the entire domain is an improvement from incorporation of swath moisture alone. Experiment TM2 produces a final pressure of 968 mb compared to SM2's 973 mb. Moisture difference plots show that both runs produce changes of equal magnitudes. The structure, however, differs significantly. Figure 32 compares the precipitable

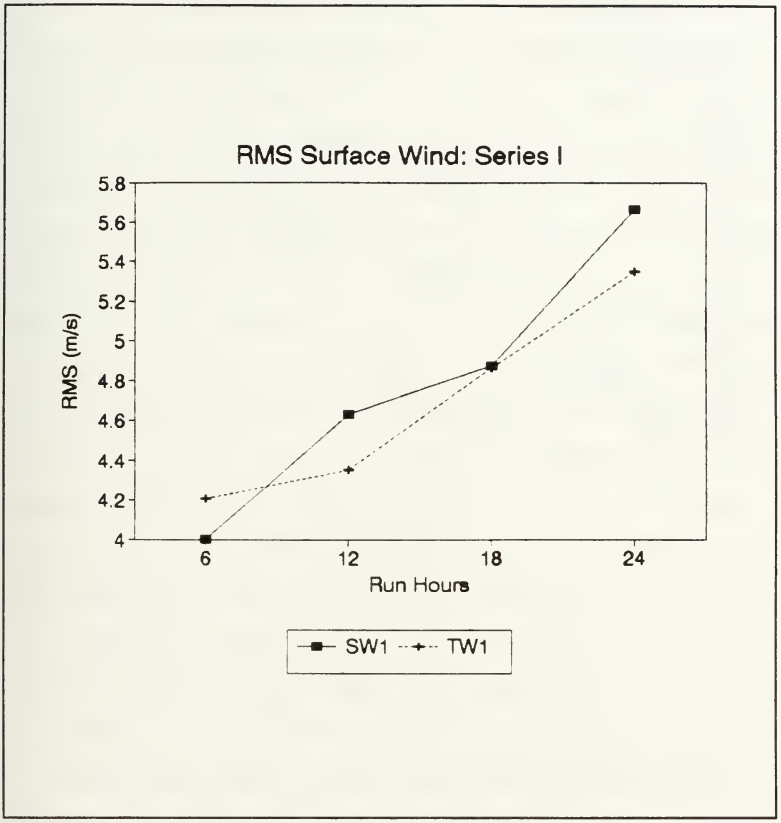

Figure 30. Series I surface wind RMS errors.

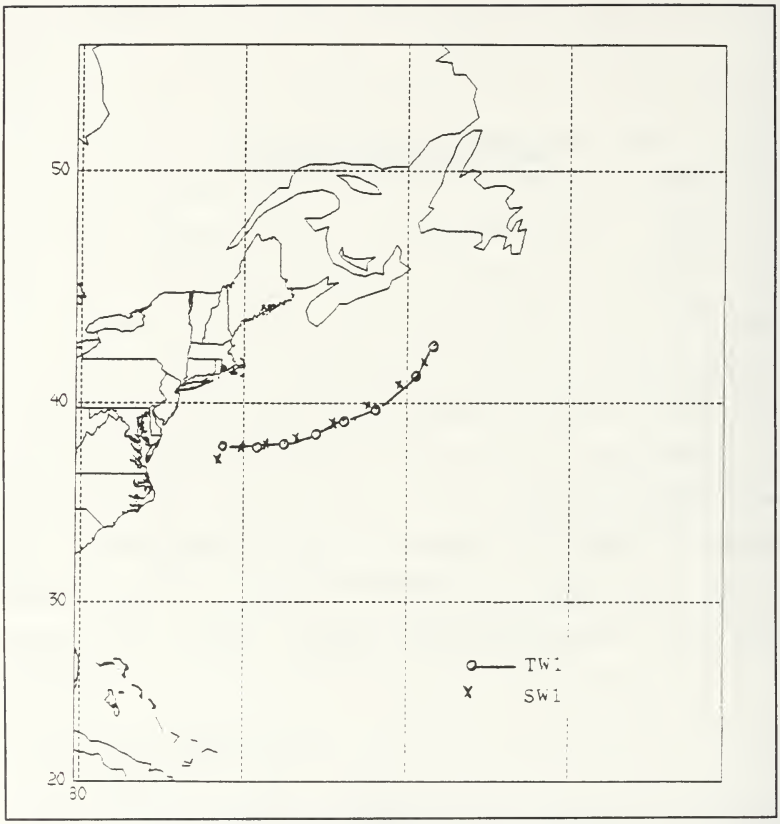

Figure 31. SW1 vs. TW1 storm tracks.

water fields for TM2 and SM2. TM2 displays a broken structure behind the cold front in the area of expected cold air advection. This may be an attempt by the model to display sub-grid scale convection. SM2 maintains a smoother integrated water pattern in the same region. The central surface pressure of the storm throughout these two experiments remains close, within 2 mb as shown in Figure 33, until the final three hours when TM2 drops 7 mb compared to SM2's 2 mb. Differences in storm structure leading up to this disparity become evident at 1800 UTC when 2400 UTC moisture values are assigned. In the swath test, Figure 34 shows temperature contours near the cold front (trailing south of the main low following the 18° and 20° C isotherms) are more closely packed in the SM2 test. The cold advection area behind the front is very jagged and disorganized. At 2100 UTC, the irregular temperature pattern in this cold advection remains, and development of the storm appears stalled. Figure 35 displays the large areal precipitation which may be associated with small scale convection in TM2.

Wind speed statistics show a marked difference between the two runs in the 500 mb wind speed field for the 1800 to 2400 UTC period. At 1800 UTC, when the 2400 UTC moisture is assigned, Figure 36 shows the a jump in RMS wind speed error for SM2 that ends up exceeding the error in the control run.

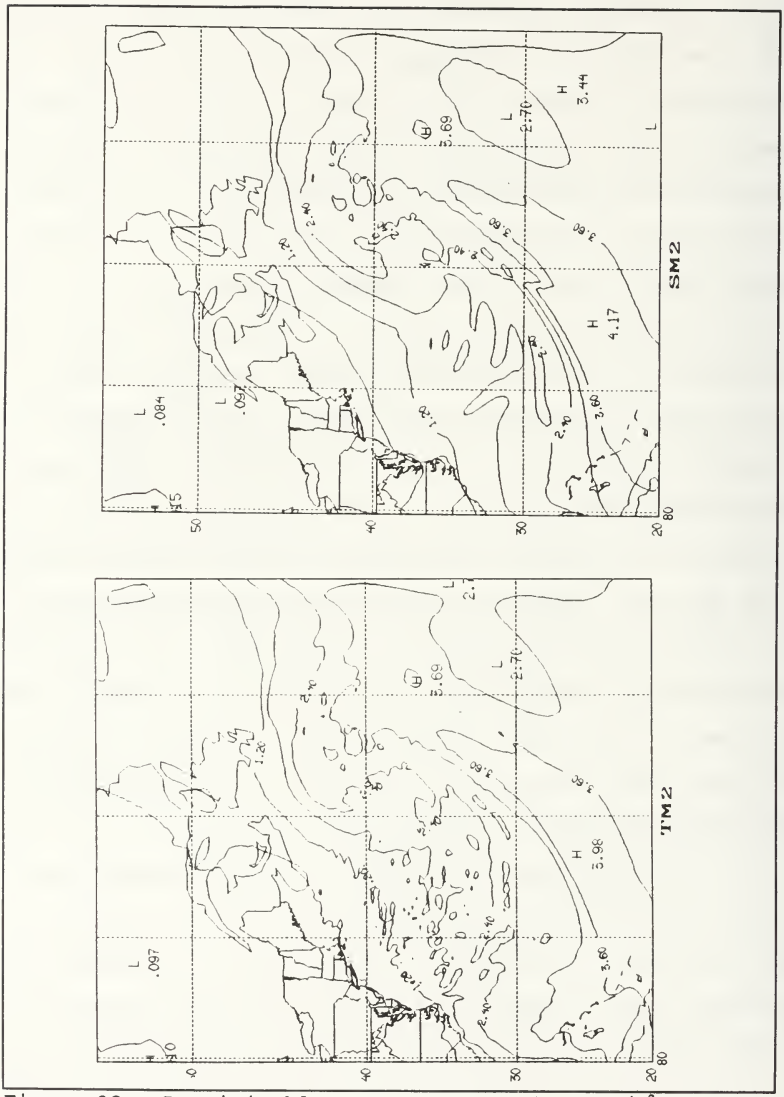

Figure 32. Precipitable water content (x10 kg/m^2) for TM2 and SM2 at 2400 UTC.

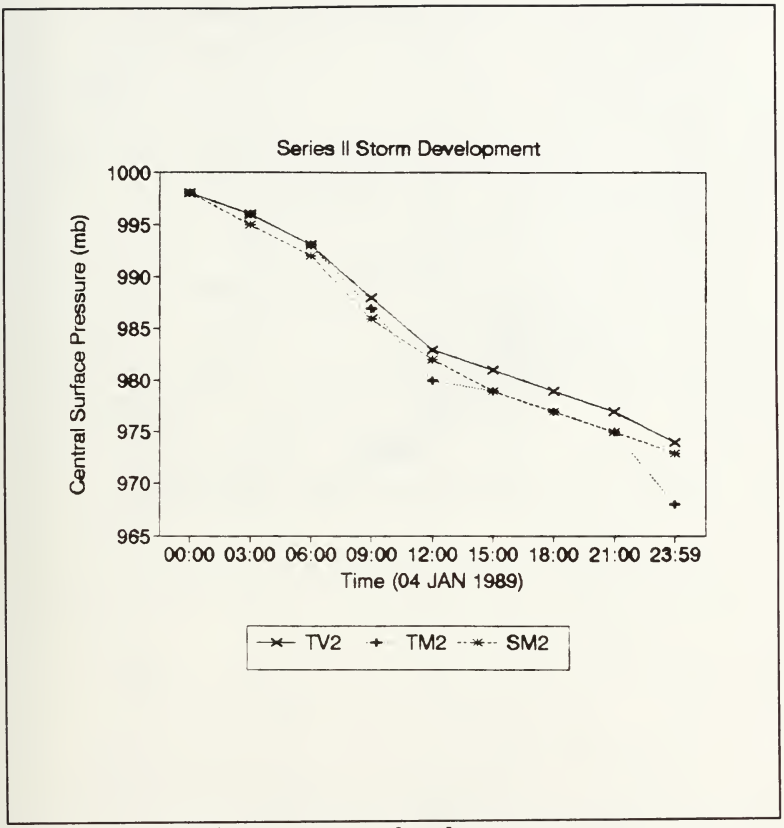

Figure 33. Series II storm development.

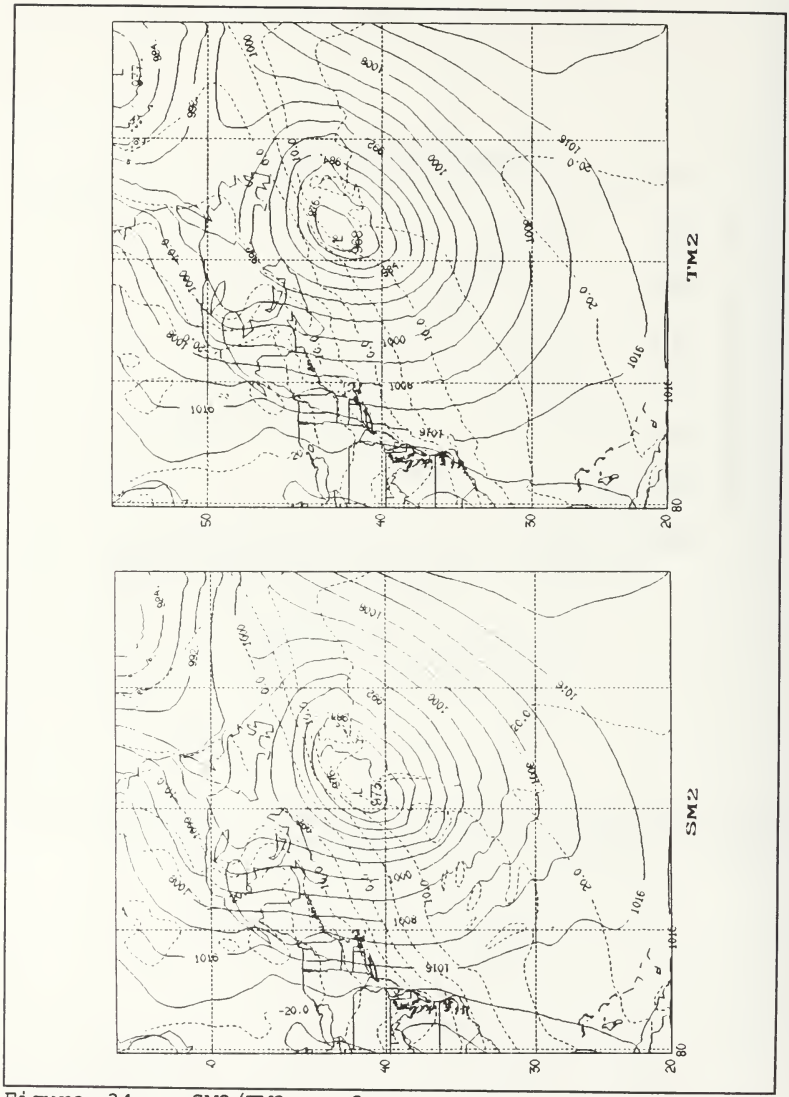

Figure 34. SM2/TM2 surface pressure (solid, mb) and temperature (dashed, °C) at 2400 UTC.

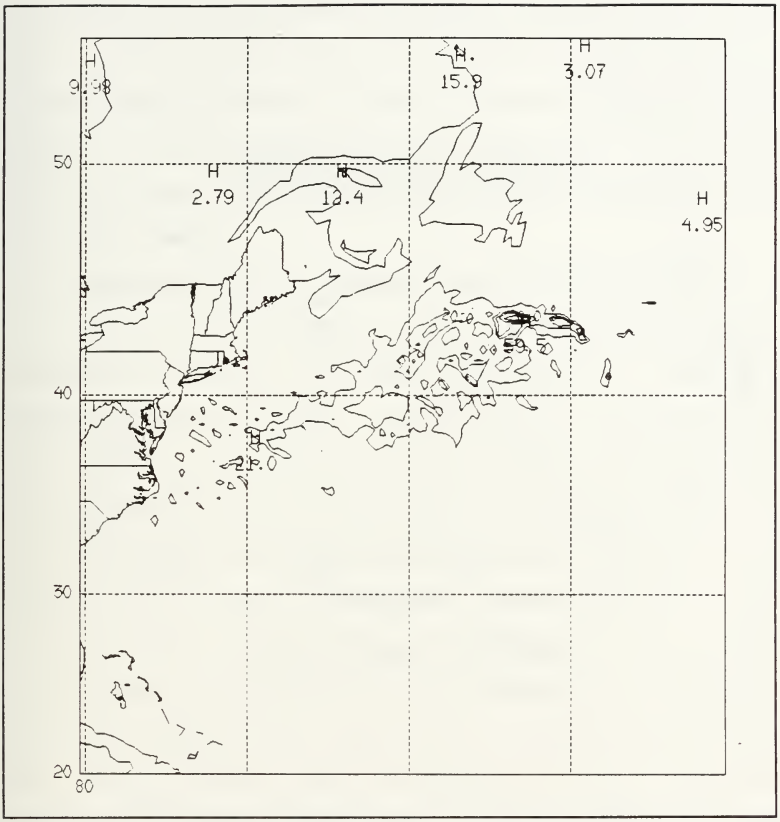

Figure 35. 24 hour accumulation of precipitation (cm) for TM2. Contour interval is 10 cm.

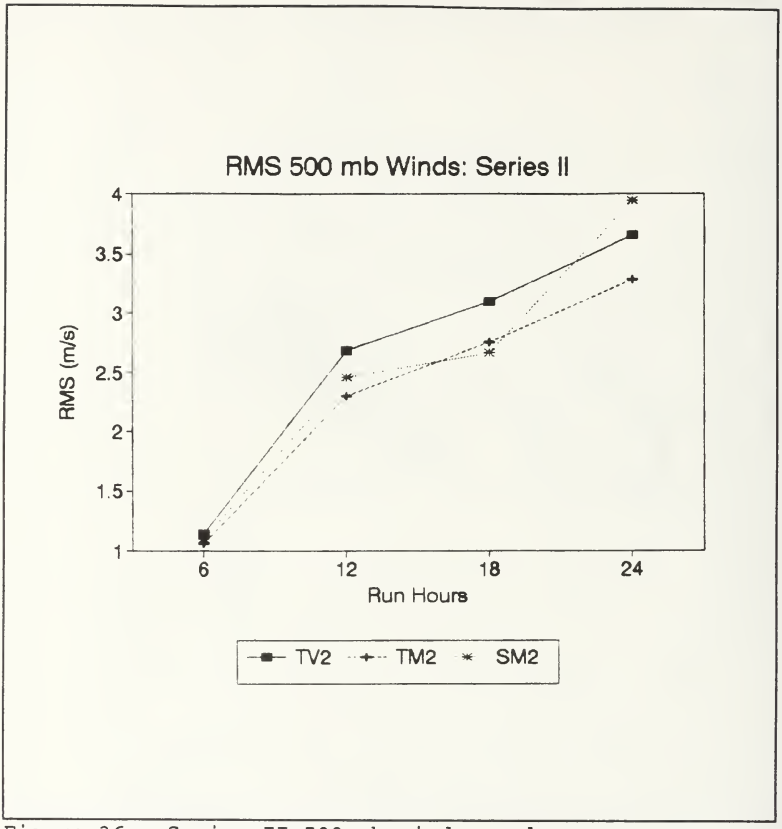

Figure 36. Series II 500 mb wind speed error.

Increasing RMS errors in 850 mb temperature also begin at 1800 UTC, but these errors do not exceed those of the control run. Finally, Figure 37 shows the 500 mb moisture fields are nearly a perfect match throughout the run in TM2. SM2, however, has errors nearly an order of magnitude greater, peaking at 1800 UTC and decreasing.

2. Surface Only vs. Vertical Moisture Distribution

Employing the vertical moisture distribution scheme described in Chapter IV slows development of the storm providing a poorer forecast. Compared to the control run, use of the vertical distribution scheme reduced the effectiveness of the moisture inputs. Both frontal moisture band structure and cold air convection are suppressed. The vertical distribution technique improves the temperature field at 850 mb, but not far above or below. Differences in the surface pressure start at 1 mb at 0900 UTC (Figure 33). During the final three hours of the experiment, the surface only test (TM2) drops 9 mb, while inclusion of the vertically distributed moisture (TV2) nets only a 3 mb drop. TV2 displays the same unsettled isotherm pattern in the cold advection region seen in earlier tests. In integrated water vapor comparisons, TV2 shows some of the mottled moisture cells, certainly a more accurate depiction than the swath test but not as accurate as TM2. TM2 suppresses the rainfall,

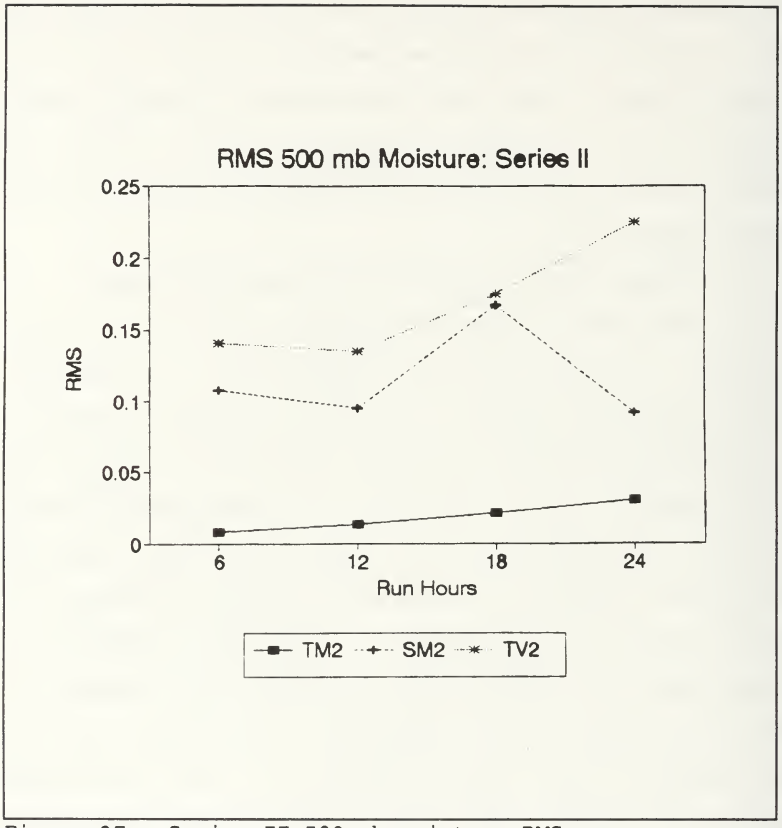

Figure 37. Series II 500 mb moisture RMS error.

reducing latent heat release and slowing development. Vertical distribution of the moisture tends to slow winds in the lower portion of the atmosphere, notably the 34 vs 30 m/s winds maxima at 900 mb, 1800 UTC in Figure 38. The RMS error for 850 mb winds of TV2 was the worst among the 9 runs, while TM2 produced the smallest errors.

Upper atmosphere temperature is sensitive to the two differing methods of determining moisture throughout the column. TV2 maintains RMS errors of temperature at 500 mb greater than the control run error (Figure not shown.) TM2 errors match the control run until 1800 UTC, and then improve dramatically. Similarly, mid-level moisture errors are magnified with the vertical distribution. At 850 mb the RMS "q" error for TV2 is worse than the control run until 1500 UTC.

As discussed in the description of the vertical distribution scheme in Chapter IV, the vertical moisture distribution scheme computes the difference in total integrated water determined by the 10 layer model and by the 16 layer model. After the individual layers in M10 are checked for saturation, the computed difference is spread over the unsaturated layers, each layer receiving a piece of the correction proportional to the layer's relative humidity for a moistening correction. Conversely, for a drying correction the amount of moisture removed from each layer is proportional to its relative humidity. The model is checked to prevent

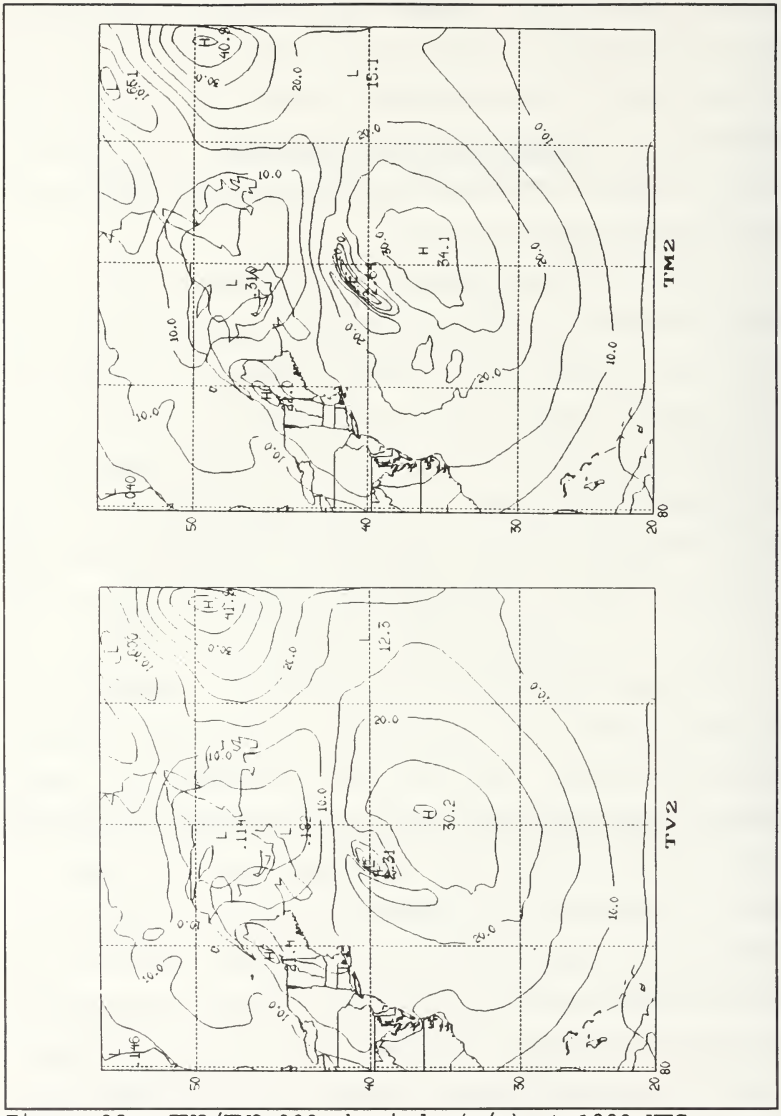

Figure 38. TV2/TM2 900 mb winds (m/s) at 1800 UTC.

removal of moisture in a layer resulting in a negative value. This scheme has the effect of restricting the moisture changes to the lowest layers (700 mb and below) of the atmosphere where the relative humidity is highest. Confining the mass changes to these lowest levels seems to have suppressed storm development by inhibiting mass and momentum transport.

E. TIME SENSITIVITY

No significant surface pressure decrease differences exist between TV2 and TV3. Structurally, a better defined cold front exists in TV3 at 1200 UTC, but the time shift does not reduce the structural changes in the cold advection region. No significant changes in moisture or rainfall coverage exist. In most of the statistical checks, TV3 matches the trends of TV2 with slightly improved errors. Notable exceptions to this include the RMS wind error at the surface. The reduced lead time experiment, TV3, again matches the trend of the long lead TV2 run, but the error is greater for the shorter lead time.

With the reduced lead time, vorticity above the boundary layer associated with the surface cyclone endures longer. Vorticity at 700 mb in TV3 goes from $79.3 \times 10^{-5} s^{-1}$ at 1800 UTC to $72.2 \times 10^{-5} s^{-1}$ at 2400 (Figure 39), while the drop is larger, from $77.7 \times 10^{-5} s^{-1}$ to $66.9 \times 10^{-5} s^{-1}$ in TV2 (Figure 40). The decreasing of above-boundary layer support contributes to the poor performance of TV2.

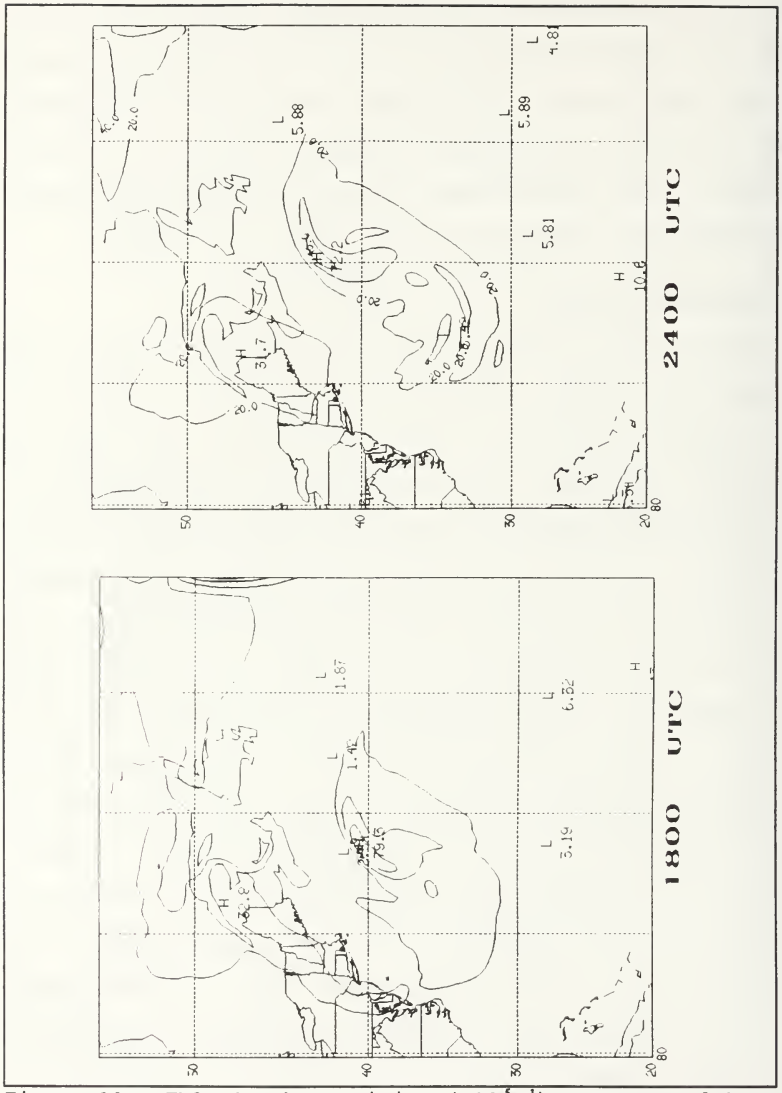

Figure 39. TV3 700 mb vorticity ($x10^{-5}s^{-1}$) at 1800 and 2400 UTC.

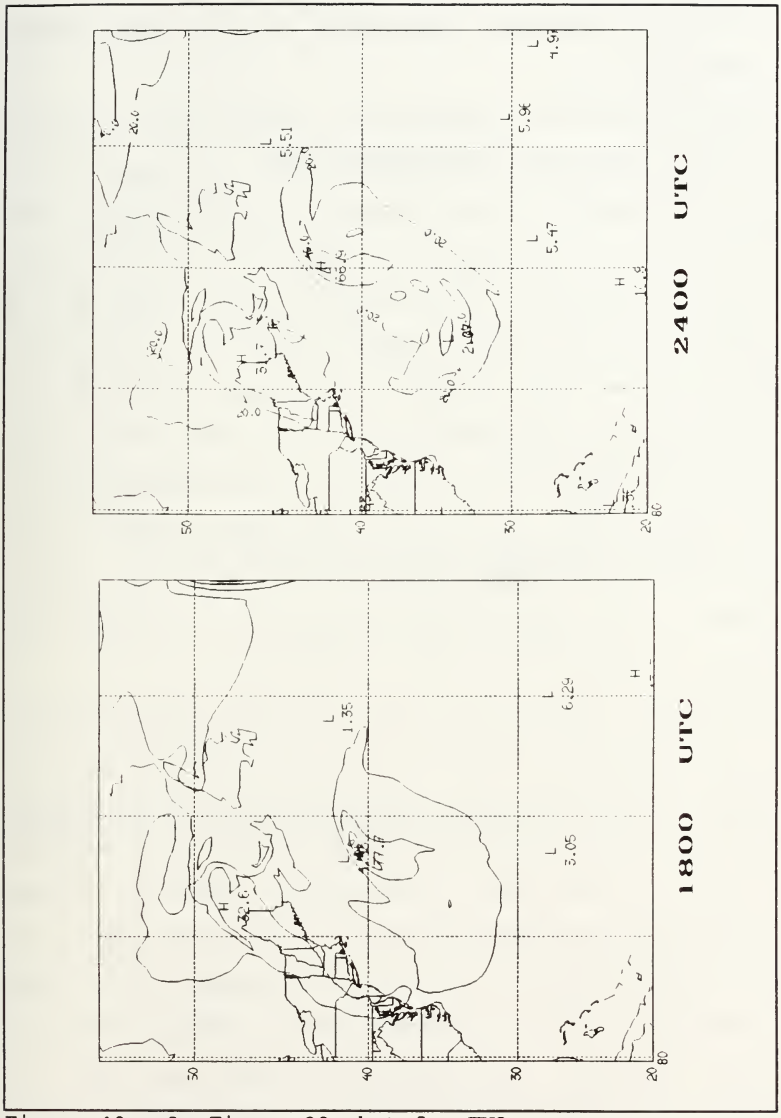

Figure 40. As Figure 39, but for TV2.

F. INDIVIDUAL PARAMETER COMPARISONS IN THE POLAR ORBITER SIMULATION

Experiment Series IV compares total domain applications of each tested parameter. The sensitivity of the model to surface wind speeds is readily apparent in this series. TW4 produces a 967 mb storm, the second best performance of the entire experiment group. Experiments TM4 and TV4 each produce a 973 mb storm, the second weakest forecast of sea level pressure in the field. Figure 41 shows the development of these three runs. TW4 improves upon the other runs almost immediately, dropping to 3 mb below the moisture experiments as early as 0600 UTC. At 1200 UTC development of TW4 slows, allowing TM4 to surpass the wind test by 1 mb. Here, development of TM4 quickly slows, while the other experiments continue to deepen.

The surface pressure and temperature plot of TW4 in Figure 42 at 0600 shows the increased area of cold advection around the western edge of the low. Good advection can be inferred from the north end of the low westward around to the southern edge, while in the other two experiments advection extends only to the south-southwestern point. At 1500 UTC (Figure not shown), determination of the cold front becomes difficult in TW4, while the 16-18 ° C isotherm packing in TM4 and TV4 makes the front obvious. Warm advection across the front is increased in the moisture runs as well. This suggests, since

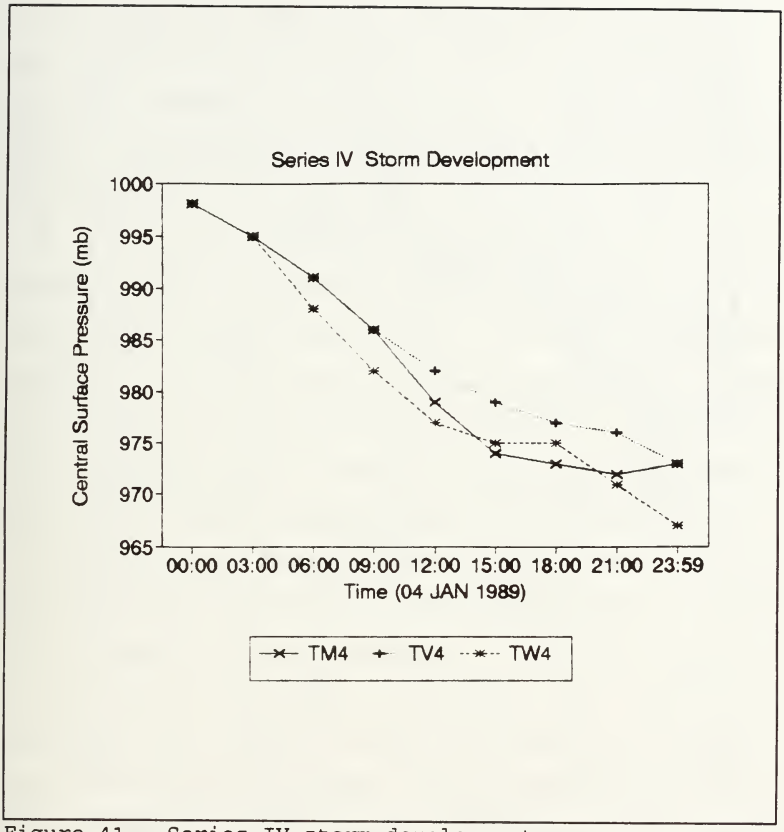

Figure 41. Series IV storm development.

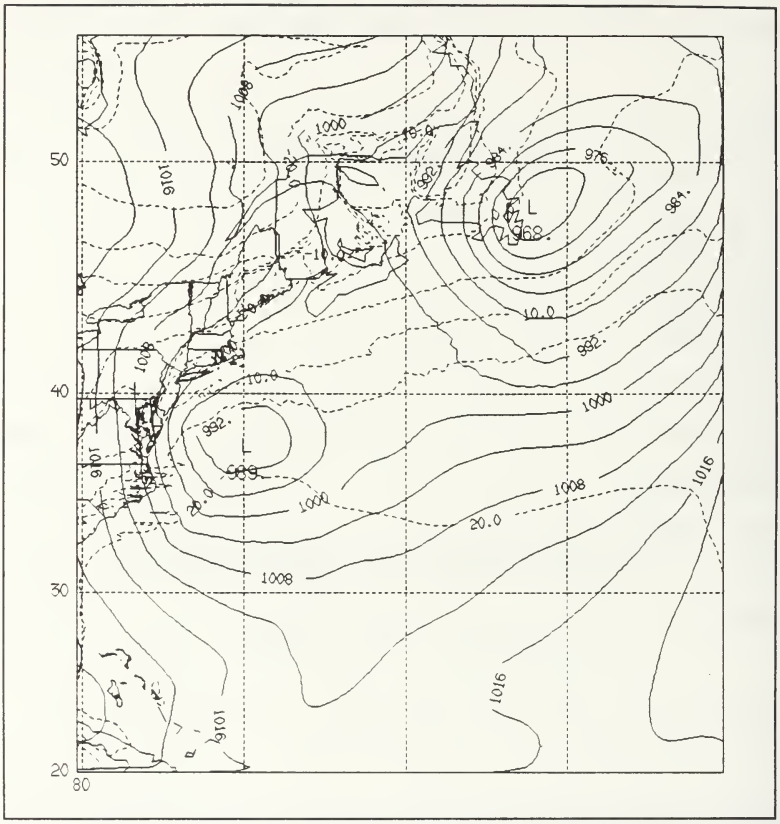

Figure 42. TW4 surface pressure (solid, mb) and temperature (dashed, °C) at 0600 UTC.

the last update by "observed" fields was with the 1200 UTC fields inserted at 0600, that the model reacts quickly to wind speed distribution and slowly (here about 9 hours) to moisture inputs. Warm advection is strongest in the vertically distributed run, TV4.

By 1800 warm air advection modeling by the TW4 run surpasses that of the moisture tests, creating a marked "S" shape baroclinic zone. Significant warm air advection occurs northeast of the low, and strong cold air advection occurs west-southwest of the low (Figure not shown). By the end of the run, TW4 has produced a storm farther north with stronger warm and cold advection, 6 mb deeper than the moisture runs.

Water vapor distribution remains similar among the three experiments until 0900 UTC. Both moisture tests show the previous patchy moisture pattern in the cold advection region. The wind test remains smooth for the first half of the experiment. The contours become disturbed but never fully achieve the mottled pattern. Total precipitation in the surface moisture run exceeds that of the vertically distributed moisture on the surface wind test.

Incorporation of the 1200 UTC observed surface winds at 0600 distorts the isotherm field in TW4 (Figure not shown). At this early stage of the storm, two nearly equal wind maxima are placed northwest and southeast of the expected storm position. The moisture experiments each place a 31.7 m/s wind max off Cape Hatteras. This distortion does not extend far

into the upper atmosphere. By 1200 UTC, the surface pattern among the three experiments are in agreement, although the vertically distributed moisture experiment produces slightly decreased wind speeds. From this point, TW4 proceeds to develop intense speed gradients around the storm, while TV4 continues to lag TM4 in magnitude.

Figures 43 through 45 show the 2400 UTC surface pressure and temperature fields in these three experiments. Cross sections (not shown) taken perpendicular to the warm and cold fronts reveal the vertical motion gradients present in the baroclinic zones. TW4 has a single intense upward motion area, while the moisture runs show multiple weaker upward motion cells. Along the warm front, however, TM4 displays the most intense vertical motion.

Statistics of the 850 mb temperature field indicate that at this level the moisture runs significantly improve model performance (Figure 46). 850 mb RMS temperature errors in the wind test are identical to the control run errors. At 500 mb, the vertically distributed moisture run quickly degrades, ending up with the largest temperature errors of the field. Again, the wind run maintains errors close to the control run. Trends of moisture errors are very erratic. While the wind and vertically distributed moisture parallel the sawtooth control pattern in Figure 47, TV4 degrades quickly to the 1800 UTC mark, improving slightly by 2400 UTC. At 850 mb, TM4 stands out as the errant run, this time showing improvement

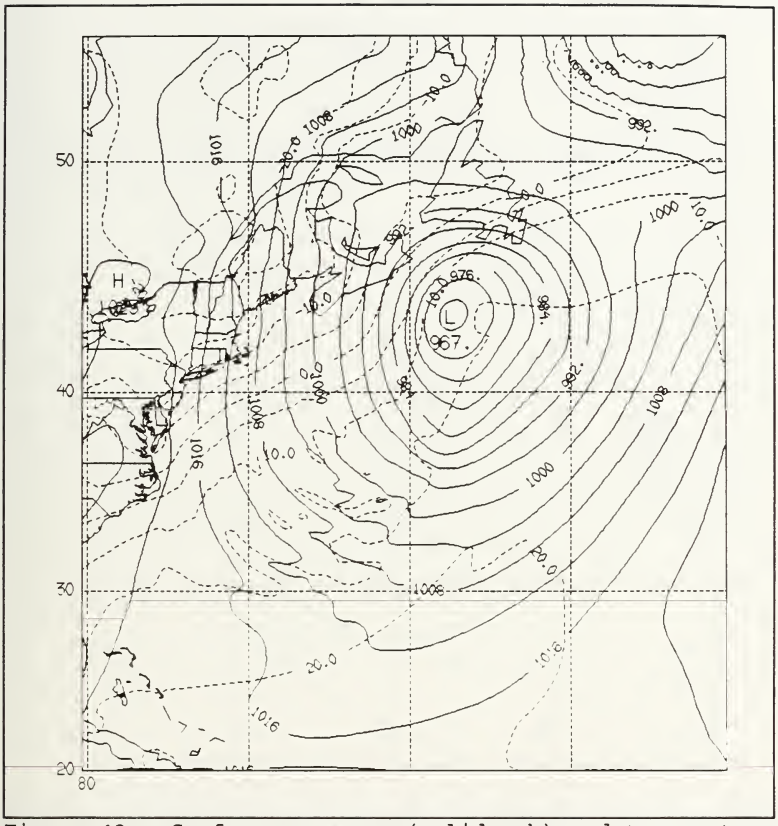

Figure 43. Surface pressure (solid, mb) and temperature (dashed, °C), TW4 at 2400 UTC.

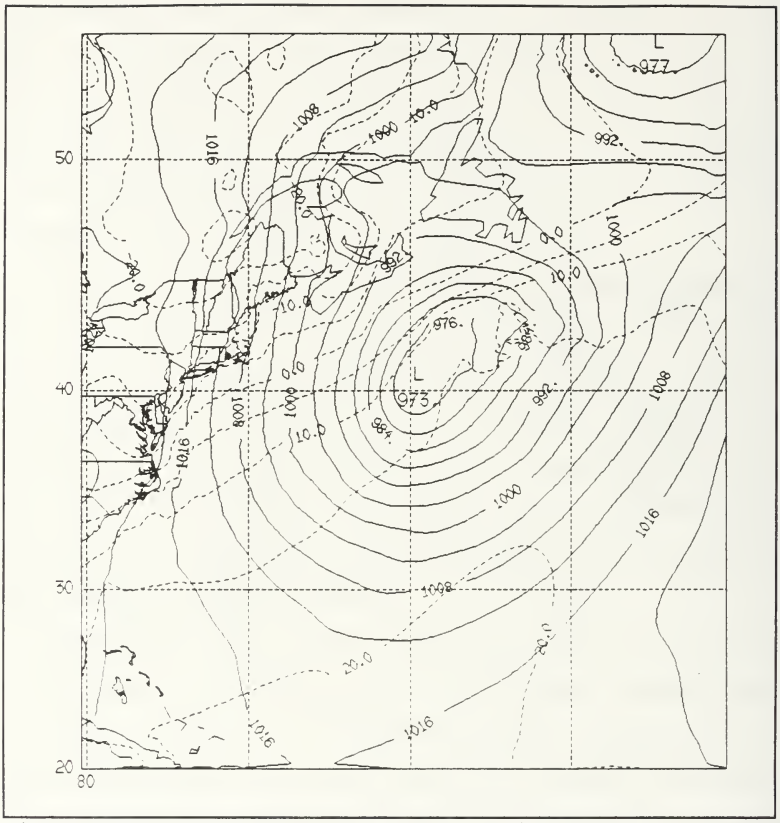

Figure 44. TM4 surface pressure (solid) and temperature (dashed), 2400 UTC.

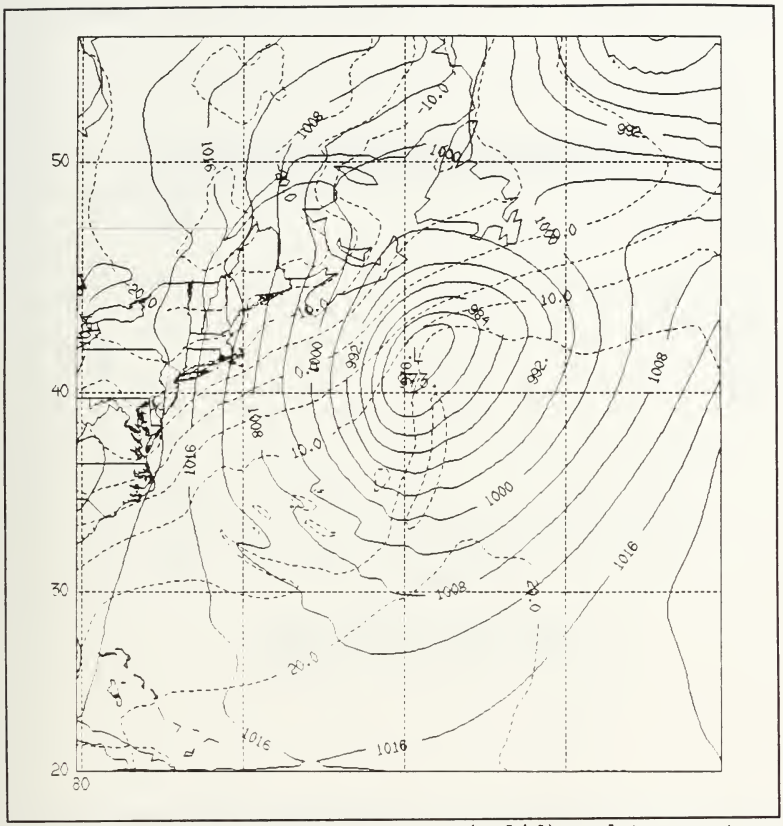

Figure 45. TV4 surface pressure (solid) and temperature (dashed), 2400 UTC.

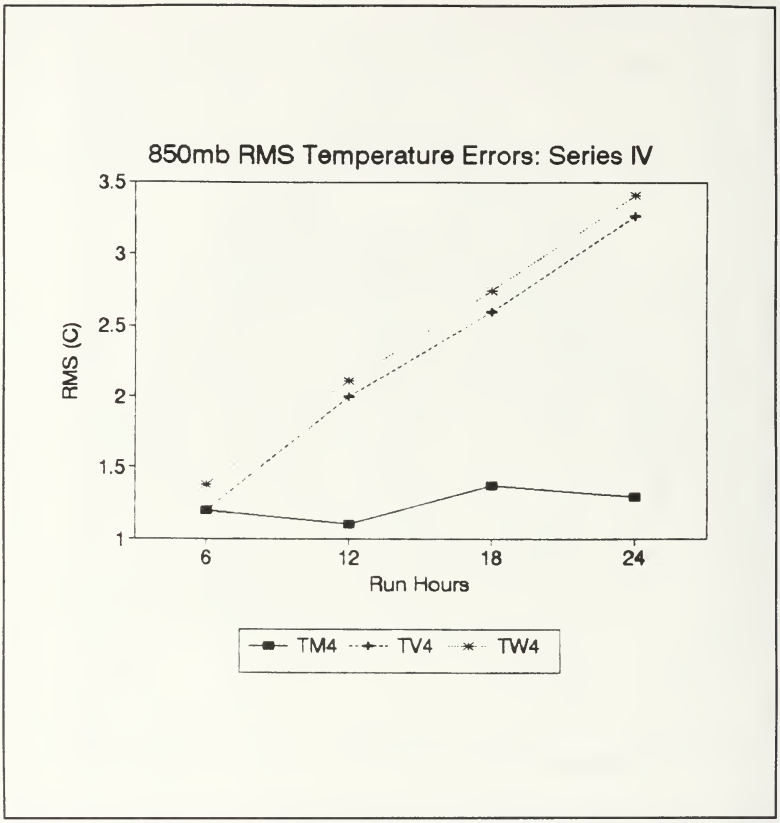

Figure 46. Series IV 850 mb temperature RMS errors.

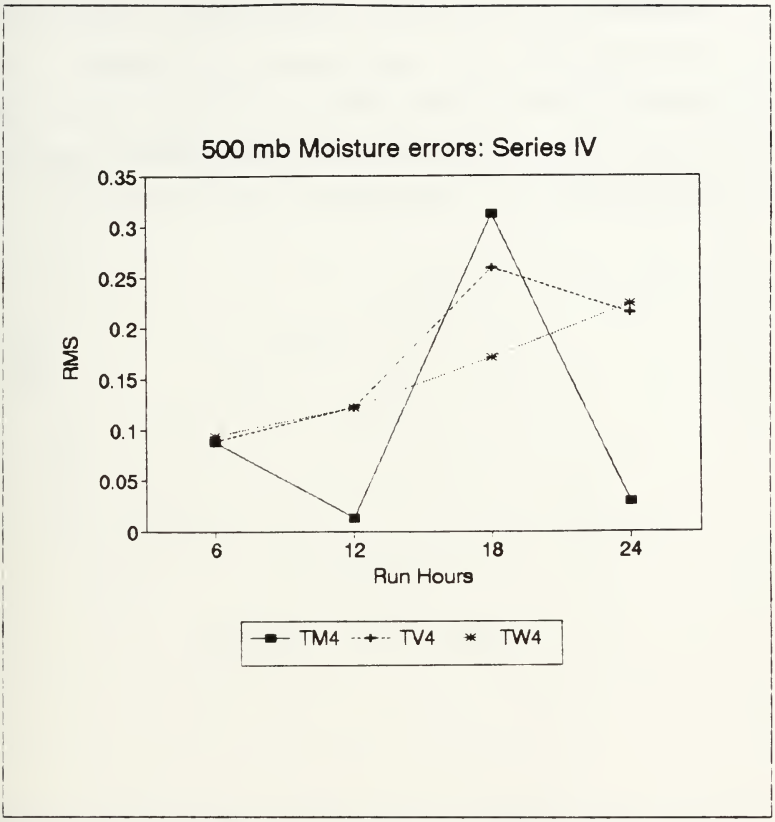

Figure 47. Series IV 500 mb moisture RMS errors.

over the control run but without a determinable trend (Figure 48). In the 500 mb level, both moisture runs spike at 1800 UTC, with TM4 improving dramatically afterwards. Finally, RMS wind errors (Figure 49) again show a 1800 UTC error peak for TM4 at the surface, with improvement by TW4 at 500 mb.

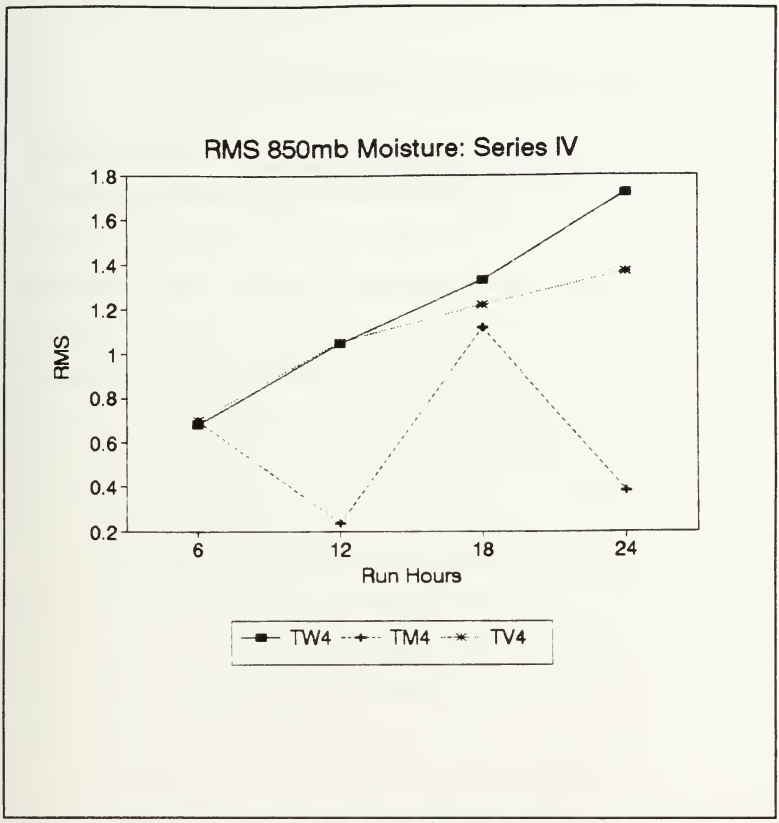

Figure 48. Series IV 850 mb moisture RMS errors.

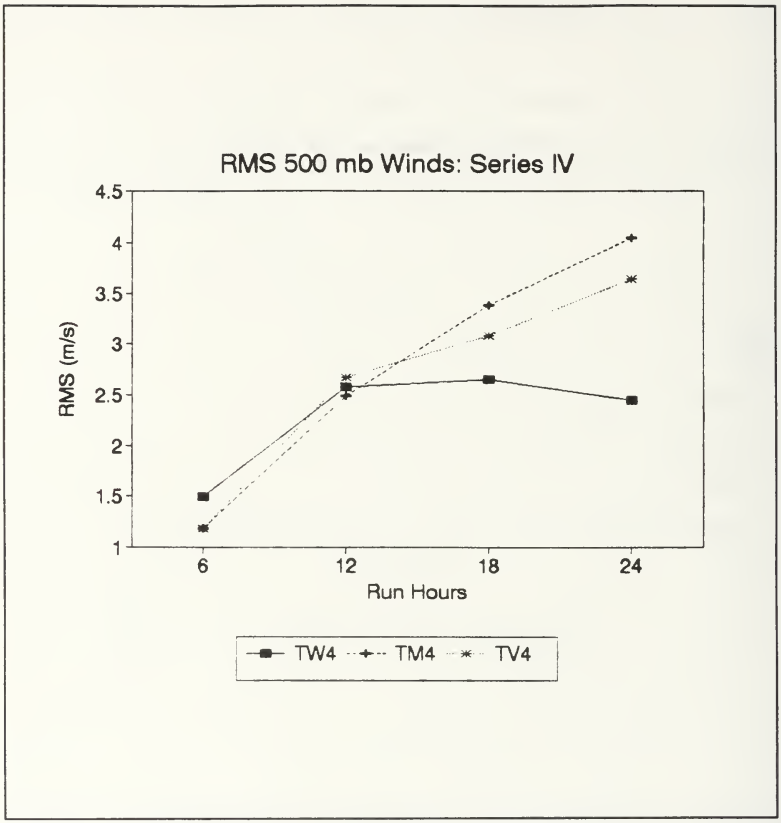

Figure 49. Series IV 500 mb wind RMS errors.

VI. CONCLUSIONS AND RECOMMENDATIONS

A. CONCLUSIONS

Without question, accurate surface wind estimates enable the NRL model to predict more accurate, deeper storms. Generally, total domain coverage with observed winds is desired, but swath winds provide significant improvements to the forecast if the swath falls over the area of main storm activity. From this information, frontal structure and temperature advection in the most important energy transfer regions can be modeled.

Incorporation of observed moisture as done in this study fails to consistently improve the prediction. Using relative humidity as a distribution variable places most of the moisture correction at the lowest levels of the atmosphere. Placement of too much moisture at the wrong levels inhibits momentum transfer and inhibits the storm development. Upper level winds decrease, reducing horizontal advection and vertical motion. The advantage of observed moisture is the improvement in open cell convection modeling as seen in the water vapor distribution fields.

Specifically, the model exhibits sensitivity to all tested parameters. Use of moisture updates enhance the structural modeling ability of M10, especially behind the cold front.

The magnitude of these corrections compared to the control run are small, not approaching the values given by the satellite images as quickly as hoped. Still, M10 itself does not produce cellular moisture structures behind the cold front without satellite information. Vertically distributing the moisture reduces the accuracy of the surface water vapor field, but improves the midlevel temperature depiction by manually redistributing the heat source poorly modeled by M10.

Assimilation of winds improves the momentum transfer from the lower levels, which has the greatest effect on the development of the storm. This carries to the upper atmosphere, as shown by the substantial improvement in 500 mb vorticity. Sensitivity to the surface winds is enhanced by strong vertical coupling of the momentum fields in M10. This coupling does not occur instantly. Based on the earlier times of the swath-domain wind experiments in Series I, the model requires about six hours to assimilate information over the domain, while local effects are evident in as little as three hours.

M10 is highly sensitive to the placement of observed data. Wind and moisture information from areas of central storm development improve the forecast. Swaths which cover more environmentally flow-controlled areas inhibit storm development by reducing gradients from storm center to the outlying environment.

The NRL model exhibits strong sensitivity to wind speeds. In this dynamic case, updating the surface momentum field carries over to heat transfer and mass continuity processes. Weaker sensitivity to moisture, which also affects heat and mass distribution, suggests that momentum fields are the most useful parameter in the modeling of the explosive cyclogenesis in this case.

B. RECOMMENDATIONS

Future studies may enjoy the opportunity of directly implanting satellite derived data into the reference atmosphere model instead of performing an OSSE. In that scenario, wind speeds obtained using current algorithms may be weighted according to the wind speed accuracies presented in Chapter II. This will allow the model to lend more credence to the most accurate winds. An algorithm or parameterization scheme may be devised to incorporate wind directions as well.

Certainly, improvements to the vertical distribution scheme are needed. Relative humidity seems to be a poor indicator to use in deciding where to place additional moisture. Other candidates include saturation mixing ratio or potential temperature. When later versions of the DMSP satellite become operational, an on-board microwave profiler will provide actual vertical moisture profiles.

LIST OF REFERENCES

Alishouse, J. C., J. B. Snider, E. R. Westwater, C. T. Swift, C. S. Ruf, S. A. Snyder, J. Vongsathorn and R. R. Ferraro, 1990a: Determination of cloud liquid water content using the SSM/I. *IEEE Trans. Geosci. Remote Sensing,* **28,** 817-821.

Alishouse, J. C., S. A. Snyder, J. Vongsathorn and R. R. Ferraro, 1990b: Determination of oceanic total precipitable water from the SSM/I. *IEEE Trans. Geosci. Remote Sensing,* **28,** 811-815.

Arakawa, A., and V. R. Lamb, 1977: Computational design of the basic dynamical process of the UCLA general circulation model. *Methods Comput. Phys.*, **17,** 173-265.

Chang, S. W., 1979: An efficient parameterization of convective and non-convective planetary boundary layers for use in numerical models. *J. Appl. Meteor.*, **18,** 1205-1215.

Fosdick, E. K., and P. J. Smith, 1991: Latent heat release in an extratropical cyclone that developed explosively over the southeastern United States. *Mon. Wea. Rev.*, **119,** 193-207.

Goerss, J. S., 1988: Global data assimilation of SSM/I wind speed measurements. *Fourth Conference on Satellite Meteorology and Oceanography,* San Diego, Amer. Meteor. Soc., 238-241.

Hartnett, E., G. Forbes and R. Hadock, 1989: ERICA Field Phase Summary. Battelle Ocean Sciences, Richland, WA.

Hollinger, J., R. Lo, and G. Poe, 1987: *Special Sensor Microwave/Imager User's Guide,* Naval Res. Lab., Washington, DC.

Hollinger, J., 1989: *DMSP Special Sensor Microwave/Imager Calibration Validation Final Report Vol. I,* Naval Res. Lab., Washington, DC.

Hollinger, J. and G. D. Sandlin, 1990: Global weather observations with SSM/I. NRL Pub. 171-8310, Naval Res. Lab., Washington, DC.

Hollinger, J., 1991: *DMSP Special Sensor Microwave/Imager Calibration Validation Final Report Vol. II,* Naval Res. Lab., Washington, DC.

Holt, T. R., S. Chang and S. Raman, 1990: A numerical study of the coastal cyclogenesis in GALE IOP 2: Sensitivity to PBL parameterizations. *Mon. Wea. Rev.*, **118,** 234-257.

Kuo, H. L., 1974: Further studies of the parameterization of the influence of cumulus convection on large-scale flow. *J. Atmos. Sci.*, **31,** 1232-1240.

Kuo, Ying-Hwa, M. A. Shapiro and E. G. Donall, 1991: The interaction between baroclinic and diabatic processes in a numerical simulation of a rapidly intensifying extratropical cyclone. *Mon. Wea. Rev.*, **119,** 368-384.

Kuo, Ying-Hwa, and S. Low-Nam, 1990: Prediction of nine explosive cyclones over the western Atlantic Ocean with a regional model. *Mon. Wea. Rev.*, **118,** 3-25.

Lipton, A. E., 1989: Observing Systems Simulation Experiments: Their Role in Meteorology. AFGL-TR-89-0097. [Available from Air Force Geophysics Laboratory, Hanscom AFB, MA. 01731.]

Madala, R.V., S. W. Chang, U. C. Mohanty, S. C. Madan, R. K. Paliwal, V. B. Sarin, T. Holt and S. Raman, 1987: Description of Naval Research Laboratory limited area dynamical weather prediction model. NRL Technical Report 5992. [Available from NRL, Washington, DC 20375.]

Nieman, P. J., M. A. Shapiro and L. S. Fedor, 1991: Synoptic and mesoscale frontal characteristics within an intense extratropical marine cyclone: ERICA IOP 4, 4-5 January 1989. *First International Symposium on Winter Storms,* New Orleans, Amer. Meteor. Soc.,108-114.

Pauley, P. A., J. E. Hoke and M. J. Pecnick, 1991: Dynamic vs. diabatic forcing of rapid cyclogenesis: Two case studies from NGM forecasts. *First International Symposium on Winter Storms,* New Orleans, Amer. Meteor. Soc., 345-350.

Poe, G. A. and R. W. Conway, 1990: A study of the geolocation errors of the Special Sensor Microwave/Imager (SSM/I). *IEEE Trans. Geosci. Remote Sensing,* **28,** 791-799.

Reynolds, R. W., 1982: Monthly averaged sea surface temperature climatology. NOAA Technical Report NWS-31. [Available from NOAA, Washington, DC 20233.]

Sanders, F., 1990: Surface analysis over the oceans-Searching for sea truth. *Wea. Forecasting*, **5,** 596-612.

Shapiro, M. A., and D. Keyser, 1990: Fronts, jet streams, and the tropopause. Palmen Memorial Vol., C. W. Newton and E. Holopainen, Eds., Amer. Meteor. Soc., 167-191.

INITIAL DISTRIBUTION LIST

1.	Defense Technical Information Center Cameron Station Alexandria, VA 22304-6145	2
2.	Library, Code 0142 Naval Postgraduate School Monterey, CA 93943-5002	2
3.	Asst. Professor T. R. Holt Naval Postgraduate School, Code MR/Ht Monterey, CA 93943-5002	1
4.	Professor C. A. Wash Naval Postgraduate School, Code MR/Wa Monterey, CA 93943-5000	1
5.	Dr. Simon W. Chang Naval Research Laboratory, Code 4220 Washington, D.C. 20375	1
6.	Dr. James Hollinger Naval Research Laboratory, Code 4211 Washington, D.C. 20375	1
7.	Glenn Sandlin Naval Research Laboratory, Code 4211 Washington, D.C. 20375	1
8.	Dr. Vincent E. Noble Naval Research Laboratory, Code 4201 Washington, D.C. 20375	1
9.	Dr. Ken Johnston Naval Research Laboratory, Code 4200 Washington, D.C. 20375	1
10.	Dr. Gary Geernaert Office of Naval Research, Code 1122MM 800 N. Quincy St. Arlington, VA. 22217-5000	1
11.	Dr. Robert Abbey Office of Naval Research, Code 1122MM 800 N. Quincy St. Arlington, VA. 22217-5000	1

12. Dr. Alan Weinstein 1
Office of Naval Research, Code 1122MM
800 N. Quincy St.
Arlington, VA. 22217-5000

13. Naval Reseach Laboratory Monterey 1
Monterey, CA 93943-5006

B44215

Thesis
S36566 Schulz
c.1 Wind speed and moisture sensitivity tests of the NRL limited area dynamical weather prediction model : an OSSE study of ERICA IOP-4.

Thesis
S36566 Schulz
c.1 Wind speed and moisture sensitivity tests of the NRL limited area dynamical weather prediction model : an OSSE study of ERICA IOP-4.

AMERICAN BINDERY

DUDLEY KNOX LIBRARY
3 2768 00018477 4